

High-order least-square-based finite-difference–finite-volume method for simulation of incompressible thermal flows on arbitrary grids

Y. Y. Liu , H. W. Zhang, L. M. Yang , and C. Shu*

Department of Mechanical Engineering, National University of Singapore 10 Kent Ridge Crescent, Singapore 119260



(Received 30 August 2019; published 20 December 2019)

In this work, a high-order (HO) least-square-based finite difference–finite volume (LSFD-FV) method together with thermal lattice Boltzmann flux solver (TLBFS) is presented for simulation of two-dimensional (2D) incompressible thermal flows on arbitrary grids. In the present method, a HO polynomial based on Taylor series expansion is applied within each control cell, where the unknown spatial derivatives at each cell center are approximated by least-square-based finite difference (LSFD) scheme. Then the recently developed TLBFS is applied to evaluate the convective and diffusive fluxes simultaneously at the cell interface by local reconstruction of thermal lattice Boltzmann solutions of the density and internal energy distribution functions. The present HO LSFD-FV method is verified and validated by 2D incompressible heat transfer problems. Numerical results indicate that the present method can be effectively and flexibly applied to solve thermal flow problems with curved boundaries on arbitrary grids. Compared with the conventional low-order finite volume method, higher efficiency and lower memory cost make the present HO method more promising for practical thermal flow problems.

DOI: [10.1103/PhysRevE.100.063308](https://doi.org/10.1103/PhysRevE.100.063308)

I. INTRODUCTION

In the computational fluid dynamics community, how to solve heat transfer problems accurately and efficiently is always an attractive research topic. Over the past few decades, considerable advances have been made in developing numerical methods for simulation of thermal flows. The representative ones are finite difference (FD), finite volume (FV), finite element (FE) methods, and the lattice Boltzmann method (LBM) [1–7]. Furthermore, based on these algorithms, various high-order (HO) methods such as the HO FV, FD, discontinuous Galerkin (DG) methods and LBM [8–20] have been proposed and widely used due to their better accuracy and efficiency. Among them, FV methods draw the most attention because of its various advantages. First, compared with FD methods and LBM, FV methods have flexibility in dealing with problems with complex geometries since the unstructured mesh can be used. Besides, FV methods obey the conservative laws fully at the cell as well as global level and they can give more accurate results on the same mesh scale than FD methods and LBM. For example, Rouboa and Monterio [21] studied the heat transfer phenomenon in complex geometry using the FD and FV methods. The results from both methods agree well with experimental measurements while slightly better results for FV method were obtained. Moreover, Goodarzi *et al.* [22] investigated the laminar natural convection heat transfer of air inside a square enclosure using both FV method and LBM. Their results confirm that the FV method requires less CPU time and yields more accurate results compared to the LBM. When it comes to FE methods

and DG methods, FE methods may be intricate for solving conservative equations and DG methods usually suffer from low computational efficiency. Therefore, FV discretization method seems to be a promising and competitive choice for solving thermal flow problems among these methods. Based on this consideration, this paper proposes a HO FV method to enrich the studies of FV methods for simulation of incompressible thermal flows.

In this study, to obtain the HO accurate numerical solution, a HO Taylor series expansion is applied within each control cell as the approximation polynomial straightforwardly, which is then substituted into the discrete form of governing equations given by FV method. The Taylor series expansion polynomial involves the solution value and its spatial derivatives at the cell center. Accordingly, the discrete form of governing equations for each control cell would involve more than one unknown (solution value and the spatial derivatives). However, there is only one discrete equation for each control cell. To resolve this not well-posed problem, the least-square-based finite difference (LSFD) scheme is used to approximate all the spatial derivatives by the solution values at the centers of the current cell and its neighboring cells. The LSFD method was proposed by Shu and his colleagues [23], which is a mesh-free method to approximate derivatives at randomly distributed points. It is an ideal approach to approximate derivatives on unstructured meshes. LSFD has been successfully applied to simulate various flow problems [24–27] with a HO of accuracy. However, due to the nature of FD discretization, there is no guarantee for its numerical discretization to be conservative if it is applied alone. Different from FD discretization, FV discretization can remain conservative at the cell and the global level. Given this, LSFD scheme is applied as a mesh-free derivative approximation

*Corresponding author: mpeshuc@nus.edu.sg

approach in the framework of FV method in this work. As a result, the combination of LSFDFV scheme and FV method can provide a simple and effective HO solver on unstructured mesh. This has been validated in the recent work of Liu *et al.* [28], which reported that the HO LSFDFV can outperform the HO k -exact FV method [29] in terms of accuracy and efficiency. On the other hand, different from the conventional second-order (2O) FV method, the trade-off of the developed HO FV method is that the time-dependent term resulting from volume integral of solution function over the control cell involves a premultiplied coefficient matrix. As shown in the paper, the resultant linear system can be solved by a point iterative method.

Apart from solution approximation within each cell, the discrete form of governing equations also involves evaluation of numerical fluxes at the cell interface. The inviscid and viscous fluxes are usually evaluated separately in the conventional methods by using smooth function interpolation or difference approximation, which is a mathematical way. For HO methods, the evaluation of viscous flux becomes more critical and the conventional approaches may increase complexity and computational effort. Compared with the mathematical reconstruction, physical reconstruction of numerical fluxes at the cell interface is more desirable as it can guarantee that the solution at the cell interface also satisfies the governing equation. The thermal lattice Boltzmann flux solver (TLBFS) [30] is implemented based on such a physical way. In TLBFS, inviscid and viscous fluxes at the cell interface are computed simultaneously using local reconstruction of solutions of the density and internal energy distribution functions from thermal lattice Boltzmann method. Through multiscale Chapman-Enskog (C-E) expansion analysis [30], it can be shown that the thermal lattice Boltzmann equation (TLBE) solution can satisfy Navier-Stokes (N-S) equations. This means that the flow variables and fluxes at the cell interface given from TLBFS also satisfy N-S equations. So far, the accuracy, robustness and efficiency of TLBFS have been proven to be good for simulation of various incompressible thermal flows [30,31]. In this work, TLBFS is adopted to evaluate numerical fluxes at the cell interface in the HO LSFDFV method. However, the original TLBFS in the work of Wang *et al.* [30] only has a 2O of accuracy. To keep the HO accuracy of flux evaluation, the streaming distance should be limited within a proper range. The details can be found in Sec. III A. Additionally, the local-coordinate system at the cell interface is introduced for convenient implementation of TLBFS on the unstructured grids.

In summary, the present HO LSFDFV method inherits the excellently conservative property and well-developed algorithm of FV discretization method. The mesh-free LSFDFV derivative approximation approach and the combination of TLBFS provide the present HO method with flexibility to handle the complex problems with curved boundaries. Additionally, TLBFS avoids the complicated viscous flux evaluation with a physical and simple technique. All the characteristics mentioned above make the present method become a straightforward and powerful tool for solving thermal flow problems. To validate the developed HO solver, a series of incompressible thermal flow benchmark tests at various Rayleigh numbers and/or with curved boundary are provided.

II. HIGH-ORDER LEAST SQUARE-BASED FINITE DIFFERENCE-FINITE VOLUME (LSFDFV) METHOD FOR 2D INCOMPRESSIBLE THERMAL FLOWS

A. Macroscopic governing equations and HO finite volume discretization

For two-dimensional (2D) incompressible thermal flows, when the density variation is small and the Mach number is low, the equations of mass, momentum and energy conservations read

$$\frac{\partial \rho}{\partial t} + \nabla \cdot (\rho \mathbf{u}) = 0, \quad (1)$$

$$\frac{\partial \rho \mathbf{u}}{\partial t} + \nabla \cdot (\rho \mathbf{u} \mathbf{u} + p \mathbf{I}) = \nu \nabla \cdot [\nabla \rho \mathbf{u} + (\nabla \rho \mathbf{u})^T] + \mathbf{f}_E, \quad (2)$$

$$\frac{\partial T}{\partial t} + \nabla \cdot (T \mathbf{u}) = \kappa \nabla^2 T, \quad (3)$$

where ρ , p , ν , κ , and T are, respectively, the density, pressure, kinematic viscosity, thermal diffusivity and temperature of fluid flow. $\mathbf{u} = (u, v)$ is the velocity vector expressed in the global Cartesian coordinate system. \mathbf{I} is the unit tensor and the external force \mathbf{f}_E represents the buoyancy force due to the nonuniform distribution of temperature field. According to the Boussinesq approximation, \mathbf{f}_E can be modelled in the following form:

$$\mathbf{f}_E = -\rho g \beta (T - T_m) \mathbf{j}, \quad (4)$$

where g denotes the gravity acceleration, \mathbf{j} is the unit vector in the y direction, T_m is the average temperature of the flow field, and β is the thermal expansion coefficient. Equations (1)–(3) can be written in a unified way as

$$\frac{\partial \mathbf{U}}{\partial t} + \nabla \cdot \mathbf{F} = \mathbf{Q}, \quad (5)$$

where the source term \mathbf{Q} , the vectors of conservative variables \mathbf{U} and flux \mathbf{F} are given by

$$\mathbf{U} = \begin{bmatrix} \rho \\ \rho u \\ \rho v \\ T \end{bmatrix}, \quad \mathbf{F} = \begin{bmatrix} F_\rho \\ F_{\rho u} \\ F_{\rho v} \\ F_T \end{bmatrix}, \quad \mathbf{Q} = \begin{bmatrix} 0 \\ 0 \\ -\rho g \beta (T - T_m) \\ 0 \end{bmatrix}. \quad (6)$$

In this work, the governing equations are discretized by FV method, where the conservative variables are defined at cell centers. The following equation can be obtained by the integral of Eq. (5) over a control cell Ω_i with application of the divergence theorem,

$$\frac{\partial}{\partial t} \int_{\Omega_i} \mathbf{U} d\Omega = - \int_{\Gamma_i} \mathbf{F} \cdot \mathbf{n} d\Gamma + \int_{\Omega_i} \mathbf{Q} d\Omega, \quad (7)$$

where Γ_i denotes the boundary of Ω_i and $\mathbf{n} = (n_x, n_y)$ is the unit normal vector of the cell interface in the Cartesian coordinate system.

Equation (7) involves the volume integral and the surface integral. In the conventional FV method, the mean theorem that assumes the flow variables being linearly distributed in the control cell is applied and the mean value is defined at the cell/surface center, which only has a second order of accuracy. In order to represent the distribution of flow variables in the control cell more precisely, the solution variable \mathbf{U} should

be approximated by a high order polynomial, which is also used to interpolate solution value at the demanded position for evaluation of numerical fluxes. In this way, a high order of

accuracy can be achieved. In this work, the solution variable \mathbf{U} is approximated by the following polynomial given from Taylor series expansion:

$$\mathbf{U}(x, y) = \mathbf{U}_i + d\mathbf{U}_i^T \tilde{\mathbf{C}}_i, \quad (8)$$

with

$$d\mathbf{U}_i^T = \left[\frac{\partial \mathbf{U}}{\partial x} \Big|_i, \frac{\partial \mathbf{U}}{\partial y} \Big|_i, \frac{\partial^2 \mathbf{U}}{\partial x^2} \Big|_i, \frac{\partial^2 \mathbf{U}}{\partial y^2} \Big|_i, \frac{\partial^2 \mathbf{U}}{\partial x \partial y} \Big|_i, \frac{\partial^3 \mathbf{U}}{\partial x^3} \Big|_i, \frac{\partial^3 \mathbf{U}}{\partial y^3} \Big|_i, \frac{\partial^3 \mathbf{U}}{\partial x^2 \partial y} \Big|_i, \frac{\partial^3 \mathbf{U}}{\partial y^2 \partial x} \Big|_i \right],$$

$$\tilde{\mathbf{C}}_i^T = \left[x^1 y^0 \Big|_i, x^0 y^1 \Big|_i, \frac{x^2 y^0}{2} \Big|_i, \frac{x^0 y^2}{2} \Big|_i, x^1 y^1 \Big|_i, \frac{x^3 y^0}{6} \Big|_i, \frac{x^0 y^3}{6} \Big|_i, \frac{x^2 y^1}{2} \Big|_i, \frac{x^1 y^2}{2} \Big|_i \right], \quad (9)$$

where the reference point (x_i, y_i) is the cell centroid of Ω_i and $x^n y^m \Big|_i = (x - x_i)^n (y - y_i)^m$. Note that the truncation error of Eq. (8) is in the order of $O(\Delta x^4, \Delta y^4)$ from Taylor series expansion, which means that the fourth order of accuracy can be achieved. By integrating Eq. (8) over the control cell Ω_i , we have

$$\int_{\Omega_i} \mathbf{U}(x, y) d\Omega = \Omega_i \mathbf{U}_i + d\mathbf{U}_i^T \mathbf{C}_i, \quad (10)$$

with

$$\mathbf{C}_i^T = \left[\overline{\overline{x^1 y^0}} \Big|_i, \overline{\overline{x^0 y^1}} \Big|_i, \frac{\overline{\overline{x^2 y^0}}}{2} \Big|_i, \frac{\overline{\overline{x^0 y^2}}}{2} \Big|_i, \overline{\overline{x^1 y^1}} \Big|_i, \frac{\overline{\overline{x^3 y^0}}}{6} \Big|_i, \frac{\overline{\overline{x^0 y^3}}}{6} \Big|_i, \frac{\overline{\overline{x^2 y^1}}}{2} \Big|_i, \frac{\overline{\overline{x^1 y^2}}}{2} \Big|_i \right], \quad (11)$$

where $\overline{\overline{x^n y^m}} \Big|_i = \int_{\Omega_i} (x - x_i)^n (y - y_i)^m d\Omega$. Clearly, Eq. (10) has ten unknowns at the cell center (one solution value, two first-order derivatives, three 2O derivatives, and four third-order derivatives) but Eq. (7) only provides one equation for each cell. Thus, the problem is not well-posed. To resolve this problem, the unknown derivatives in Eq. (8) will be approximated by the mesh-free LSF method, which will be described in Sec. II B. The volume integral term involving the source term Q in Eq. (7) can also be computed using Eq. (10) straightforwardly. Apart from the volume integral, the surface integral in Eq. (7) also requires HO approximation. In this work, Gaussian quadrature is applied to approximate the surface integral with the fourth-order of accuracy by two Gaussian quadrature points. In this way, the surface integral in Eq. (7) can be approximated by

$$\int_{\Gamma_i} \mathbf{F} \cdot \mathbf{n} d\Gamma = \sum_{\text{edge}=1}^{\text{nedge}} \sum_{GQp=1}^{nGQp} (\mathbf{F}_{\text{edge},GQp} \cdot \mathbf{n}_{\text{edge}}) A_{\text{edge}} w_{GQp}, \quad (12)$$

where nedge is the number of surfaces for the control cell Ω_i , $nGQp$ denotes the number of Gaussian quadrature points on each control surface, w is a quadrature weight, and A is the surface area. Section II B describes how to evaluate numerical flux \mathbf{F} in Eq. (12). With Eqs. (10) and (12), Eq. (7) is reduced to a set of ordinary differential equations, whose solution will be discussed in Sec. II D.

B. Least square-based finite difference (LSFD) scheme for derivative approximation

In fact, LSF is also based on 2D Taylor series expansion as shown in Eq. (8). The derivatives are considered as unknowns and thus the number of unknowns is 9. To construct the same amount of equations as that of unknowns, Eq. (8) is applied at nine neighboring points as follows:

$$\widehat{\mathbf{S}} d\mathbf{U} = \Delta \widehat{\mathbf{U}}, \quad (13)$$

with the matrix $\widehat{\mathbf{S}}$ and $\Delta \widehat{\mathbf{U}}$ given by

$$\widehat{\mathbf{S}} = \begin{pmatrix} \Delta x_1 & \Delta y_1 & \frac{\Delta x_1^2}{2} & \frac{\Delta y_1^2}{2} & \Delta x_1 \Delta y_1 & \frac{\Delta x_1^3}{6} & \frac{\Delta y_1^3}{6} & \frac{\Delta x_1^2 \Delta y_1}{2} & \frac{\Delta y_1^2 \Delta x_1}{2} \\ \Delta x_2 & \Delta y_2 & \frac{\Delta x_2^2}{2} & \frac{\Delta y_2^2}{2} & \Delta x_2 \Delta y_2 & \frac{\Delta x_2^3}{6} & \frac{\Delta y_2^3}{6} & \frac{\Delta x_2^2 \Delta y_2}{2} & \frac{\Delta y_2^2 \Delta x_2}{2} \\ \vdots & \vdots \\ \Delta x_9 & \Delta y_9 & \frac{\Delta x_9^2}{2} & \frac{\Delta y_9^2}{2} & \Delta x_9 \Delta y_9 & \frac{\Delta x_9^3}{6} & \frac{\Delta y_9^3}{6} & \frac{\Delta x_9^2 \Delta y_9}{2} & \frac{\Delta y_9^2 \Delta x_9}{2} \end{pmatrix},$$

$$\Delta \widehat{\mathbf{U}}^T = [\mathbf{U}_{i1} - \mathbf{U}_i, \mathbf{U}_{i2} - \mathbf{U}_i, \dots, \mathbf{U}_{i9} - \mathbf{U}_i], \quad (14)$$

where $(\Delta x_j, \Delta y_j) = (x_j - x_i, y_j - y_i)$, \mathbf{U}_{ij} denotes the solution value at the center of the j th neighboring cell to the current cell i . By solving linear system (13), the derivative vector $d\mathbf{U}$ can be obtained in terms of $\Delta \widehat{\mathbf{U}}$. However, due to unstructured cell distribution for a general case, the linear system may be ill-conditioned or even singular. To overcome this difficulty, the local scaling technique and least-square optimization were used. As reported in the work of Ding *et al.* [23], by applying

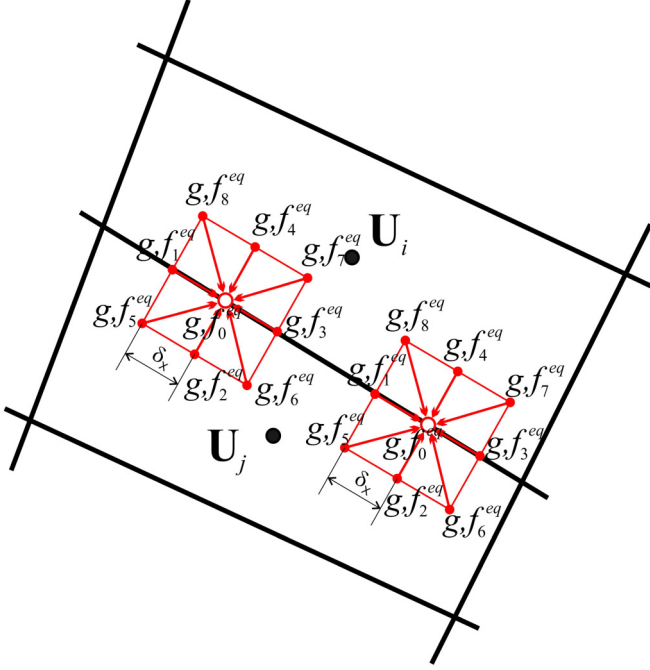


FIG. 1. Evaluation of fluxes at cell interface.

directions of the cell interface. f_α^{eq} denotes the equilibrium density distribution function along the α direction and f_α^{neq} is the corresponding nonequilibrium distribution function. g_α^{eq} denotes the equilibrium internal energy distribution function along the α direction and g_α^{neq} is the corresponding nonequilibrium distribution function. Nd is the number of discrete particle velocities in the lattice Boltzmann method. In this work, the D2Q9 model, i.e., $Nd = 9$, is applied for the density and internal energy distribution functions.

The equilibrium density distribution function f_α^{eq} and equilibrium internal energy distribution function g_α^{eq} read

$$f_\alpha^{\text{eq}} = \rho w_\alpha \left[1 + \frac{\mathbf{e}_\alpha \cdot \mathbf{u}}{c_s^2} + \frac{(\mathbf{e}_\alpha \cdot \mathbf{u})^2 - (c_s |\mathbf{u}|)^2}{2c_s^4} \right], \quad (28)$$

$$g_\alpha^{\text{eq}} = \begin{cases} -\frac{2}{9} \frac{T |\mathbf{u}|^2}{c_s^2}, & \alpha = 0 \\ \frac{T}{9} \left[\frac{3}{2} + \frac{1}{2} \cdot \frac{\mathbf{e}_\alpha \cdot \mathbf{u}}{c_s^2} + \frac{1}{2} \cdot \frac{(\mathbf{e}_\alpha \cdot \mathbf{u})^2}{c_s^4} - \frac{1}{2} \cdot \frac{|\mathbf{u}|^2}{c_s^2} \right], & \alpha = 1, 2, 3, 4. \\ \frac{T}{36} \left[3 + 2 \cdot \frac{\mathbf{e}_\alpha \cdot \mathbf{u}}{c_s^2} + \frac{1}{2} \cdot \frac{(\mathbf{e}_\alpha \cdot \mathbf{u})^2}{c_s^4} - \frac{1}{2} \cdot \frac{|\mathbf{u}|^2}{c_s^2} \right], & \alpha = 5, 6, 7, 8 \end{cases} \quad (29)$$

For D2Q9 model defined in a square lattice as shown in Fig. 1, the sound speed c_s and the coefficients w_α are given as

$$\varphi(\mathbf{r} - \mathbf{e}_\alpha \delta_t) = \begin{cases} \varphi(\mathbf{r}_i) + \nabla \varphi(\mathbf{r}_i) \Delta \mathbf{X}_i + \frac{1}{2} \Delta^2 \mathbf{X}_i^T \mathbf{H}(\mathbf{X}_i) \Delta \mathbf{X}_i & (\mathbf{r} - \mathbf{e}_\alpha \delta_t) \in \Omega_i \\ + \frac{1}{6} \Delta^2 \mathbf{X}_i^T \mathbf{G}(\mathbf{X}_i) \Delta \mathbf{X}_i + O(X^4), & \\ \varphi(\mathbf{r}_j) + \nabla \varphi(\mathbf{r}_j) \Delta \mathbf{X}_j + \frac{1}{2} \Delta^2 \mathbf{X}_j^T \mathbf{H}(\mathbf{X}_j) \Delta \mathbf{X}_j & (\mathbf{r} - \mathbf{e}_\alpha \delta_t) \in \Omega_j \\ + \frac{1}{6} \Delta^2 \mathbf{X}_j^T \mathbf{G}(\mathbf{X}_j) \Delta \mathbf{X}_j + O(X^4), & \end{cases}$$

$$\text{where } \varphi = \begin{pmatrix} \rho \\ \mathbf{u} \\ T \end{pmatrix}, \quad \Delta \mathbf{X}_i = \begin{pmatrix} (\mathbf{r} - \mathbf{e}_\alpha \delta_t - \mathbf{r}_i)_x \\ (\mathbf{r} - \mathbf{e}_\alpha \delta_t - \mathbf{r}_i)_y \end{pmatrix}, \quad \Delta \mathbf{X}_j = \begin{pmatrix} (\mathbf{r} - \mathbf{e}_\alpha \delta_t - \mathbf{r}_i)_x \\ (\mathbf{r} - \mathbf{e}_\alpha \delta_t - \mathbf{r}_i)_y \end{pmatrix}$$

$$\Delta^2 \mathbf{X}_i^T = ((\mathbf{r} - \mathbf{e}_\alpha \delta_t - \mathbf{r}_i)_x^2, (\mathbf{r} - \mathbf{e}_\alpha \delta_t - \mathbf{r}_i)_y^2),$$

$$\Delta^2 \mathbf{X}_j^T = ((\mathbf{r} - \mathbf{e}_\alpha \delta_t - \mathbf{r}_i)_x^2, (\mathbf{r} - \mathbf{e}_\alpha \delta_t - \mathbf{r}_i)_y^2). \quad (35)$$

$c_s = c/\sqrt{3}$, $w_0 = 4/9$, $w_1 = w_2 = w_3 = w_4 = 1/9$, and $w_5 = w_6 = w_7 = w_8 = 1/36$. $c = \delta_x/\delta_t$. δ_x and δ_t denote the lattice spacing and the streaming time step, respectively. Generally, c is taken as 1.

The kinematic viscosity ν and thermal diffusivity κ can be estimated, respectively, from the relaxation parameters τ_ν and τ_κ with

$$\nu = (\tau_\nu - \frac{1}{2}) c_s^2 \delta_t, \quad (30)$$

$$\kappa = 2(\tau_\kappa - \frac{1}{2}) c_s^2 \delta_t. \quad (31)$$

The pressure can be calculated from the equation of state,

$$p = \rho c_s^2. \quad (32)$$

The nonequilibrium distribution functions f_α^{neq} in Eqs. (25) and (26) and g_α^{neq} in Eq. (27) can be approximated by

$$f_\alpha^{\text{neq}}(\mathbf{r}, t) = -\tau_\nu [f_\alpha^{\text{eq}}(\mathbf{r}, t) - f_\alpha^{\text{eq}}(\mathbf{r} - \mathbf{e}_\alpha \delta_t, t - \delta_t)] + O(\delta_t^2), \quad (33)$$

$$g_\alpha^{\text{neq}}(\mathbf{r}, t) = -\tau_\kappa [g_\alpha^{\text{eq}}(\mathbf{r}, t) - g_\alpha^{\text{eq}}(\mathbf{r} - \mathbf{e}_\alpha \delta_t, t - \delta_t)] + O(\delta_t^2), \quad (34)$$

where \mathbf{r} is physical location and t is time. $f_\alpha^{\text{eq}}(\mathbf{r}, t)$ and $f_\alpha^{\text{eq}}(\mathbf{r} - \mathbf{e}_\alpha \delta_t, t - \delta_t)$ are the equilibrium density distribution functions at the Gaussian quadrature point \mathbf{r} along the cell interface and its surrounding nodes $\mathbf{r} - \mathbf{e}_\alpha \delta_t$, respectively. $g_\alpha^{\text{eq}}(\mathbf{r}, t)$ and $g_\alpha^{\text{eq}}(\mathbf{r} - \mathbf{e}_\alpha \delta_t, t - \delta_t)$ are the equilibrium internal energy distribution functions at the corresponding positions. Note that, since $c = 1$, the streaming time step δ_t equals the lattice spacing δ_x . Equations (33) and (34) indicate that TLBFS has the 2O of accuracy in terms of the lattice spacing δ_x rather than the mesh spacing Δx . In practical implementation, δ_x is chosen to be much smaller than Δx in order to keep the global accuracy of the solution.

In order to calculate $f_\alpha^{\text{neq}}(\mathbf{r}, t)$, we have to obtain $f_\alpha^{\text{eq}}(\mathbf{r}, t)$ and $f_\alpha^{\text{eq}}(\mathbf{r} - \mathbf{e}_\alpha \delta_t, t - \delta_t)$ first. Similarly, $g_\alpha^{\text{eq}}(\mathbf{r}, t)$ and $g_\alpha^{\text{eq}}(\mathbf{r} - \mathbf{e}_\alpha \delta_t, t - \delta_t)$ should be computed first, then $g_\alpha^{\text{neq}}(\mathbf{r}, t)$ can be got from Eq. (34). For $f_\alpha^{\text{eq}}(\mathbf{r} - \mathbf{e}_\alpha \delta_t, t - \delta_t)$ and $g_\alpha^{\text{eq}}(\mathbf{r} - \mathbf{e}_\alpha \delta_t, t - \delta_t)$, the corresponding fluid density ρ , velocity \mathbf{u} and temperature T can be given from those at cell center via the HO polynomial approximation form (8). As an example, based on the information at cell centroids \mathbf{r}_i and \mathbf{r}_j and according to Eq. (8), any variable φ at the location $(\mathbf{r} - \mathbf{e}_\alpha \delta_t)$ can be interpolated as

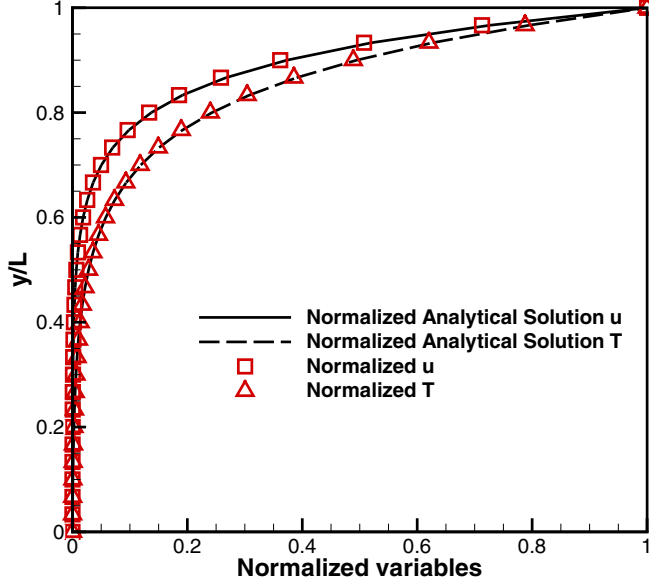


FIG. 2. Velocity and temperature profiles obtained by HO LSFDFV method using TLBFS for porous plate problem at $Pr = 0.71$, $Re = 10$, and $Ra = 100$.

The gradient $\nabla\varphi$, the matrices \mathbf{H} and \mathbf{G} are

$$\nabla\varphi = \left(\frac{\partial\varphi}{\partial x}, \frac{\partial\varphi}{\partial y} \right),$$

$$\mathbf{H} = \begin{bmatrix} \frac{\partial^2\varphi}{\partial x^2} & \frac{\partial^2\varphi}{\partial x\partial y} \\ \frac{\partial^2\varphi}{\partial y\partial x} & \frac{\partial^2\varphi}{\partial y^2} \end{bmatrix}, \quad \mathbf{G} = \begin{bmatrix} \frac{\partial^3\varphi}{\partial x^3} & 3\frac{\partial^3\varphi}{\partial x^2\partial y} \\ 3\frac{\partial^3\varphi}{\partial y^2\partial x} & \frac{\partial^3\varphi}{\partial y^3} \end{bmatrix}, \quad (36)$$

where the derivatives are approximated by the LSFDFV method as introduced in Sec. II B. Once the required ρ , \mathbf{u} , and T are available, $f_\alpha^{\text{eq}}(\mathbf{r} - \mathbf{e}_\alpha\delta_t, t - \delta_t)$ and $g_\alpha^{\text{eq}}(\mathbf{r} - \mathbf{e}_\alpha\delta_t, t - \delta_t)$ can be computed from Eqs. (28) and (29), respectively. Moreover, following the derivations in Ref. [30], we can obtain

$$\rho(\mathbf{r}, t) = \sum_{\alpha=0}^{Nd} f_\alpha^{\text{eq}}(\mathbf{r} - \mathbf{e}_\alpha\delta_t, t - \delta_t), \quad (37)$$

$$\rho(\mathbf{r}, t)\mathbf{u}(\mathbf{r}, t) = \sum_{\alpha=0}^{Nd} f_\alpha^{\text{eq}}(\mathbf{r} - \mathbf{e}_\alpha\delta_t, t - \delta_t)\mathbf{e}_\alpha, \quad (38)$$

$$T(\mathbf{r}, t) = \sum_{\alpha=0}^{Nd} g_\alpha^{\text{eq}}(\mathbf{r} - \mathbf{e}_\alpha\delta_t, t - \delta_t). \quad (39)$$

Thus, $f_\alpha^{\text{eq}}(\mathbf{r}, t)$ and $g_\alpha^{\text{eq}}(\mathbf{r}, t)$ can be, respectively, calculated by Eqs. (28) and (29). Then, $f_\alpha^{\text{neq}}(\mathbf{r}, t)$ can be calculated by Eq. (33) and $g_\alpha^{\text{neq}}(\mathbf{r}, t)$ can be computed by Eq. (34). Finally, all the fluxes F_{ρ_1} , $F_{\rho u_1}$, $F_{\rho u_2}$, and F_{T_1} in Eqs. (24)–(27) can be obtained.

Since the fluxes in Eqs. (24)–(27) are defined in the local-coordinate system, they cannot be used in Eq. (5) directly. We have to conduct the coordinate transformation as the following equation, then the fluxes \mathbf{F} in the global Cartesian coordinate system can be evaluated:

$$\mathbf{F} = (F_{\rho_1}, F_{\rho u_1}n_x - F_{\rho u_2}n_y, F_{\rho u_2}n_x + F_{\rho u_1}n_y, F_{T_1})^T. \quad (40)$$

TABLE I. Accuracy test results of temperature T for the porous plate problem.

Scheme	Mesh size	Quadrilateral Mesh		Triangular Mesh	
		L_1 errors	Order	L_1 errors	Order
HO	1/5	2.17×10^{-1}		3.08×10^{-2}	
	1/10	1.77×10^{-2}	3.619	2.83×10^{-3}	3.445
	1/20	1.37×10^{-3}	3.691	3.05×10^{-4}	3.212
	1/30	3.42×10^{-4}	3.419	9.76×10^{-5}	2.814
2O	1/10	5.16×10^{-1}		1.37×10^{-1}	
	1/20	1.20×10^{-1}	2.107	3.41×10^{-2}	2.002
	1/30	5.22×10^{-2}	2.049	1.56×10^{-2}	1.932
	1/40	2.92×10^{-2}	2.016	9.40×10^{-3}	1.760

Note that, in TLBFS, the LBE solution is reconstructed physically and locally at every Gaussian quadrature point along each cell interface. This means that different δ_x could be chosen for different interfaces, which provides great flexibility for application on unstructured grids. Meanwhile, due to the independence between the time marching step Δt and the streaming time step δ_t (δ_t is only used in the solution reconstruction), the choice of small δ_x will not affect the time evolution process in the present method.

D. Solution of resultant ordinary differential equations

By substituting the derivative expression of Eq. (23) approximated by LSFDFV method into Eq. (10), we have

$$\begin{aligned} \int_{\Omega_i} \mathbf{U}(x, y) d\Omega &= \Omega_i \mathbf{U}_i + \sum_{k=1}^9 C_k d\mathbf{U}_k \\ &= \Omega_i \mathbf{U}_i + \sum_{k=1}^9 C_k \sum_{j=1}^N W_{k,j} \Delta \mathbf{U}_{ij} \\ &= \Omega_i \mathbf{U}_i + \sum_{k=1}^9 C_k \sum_{j=1}^N W_{k,j} (\mathbf{U}_{ij} - \mathbf{U}_i). \end{aligned} \quad (41)$$

For the whole domain, Eq. (41) is applied to each control cell. It is noteworthy that the coefficients C_k and $W_{k,j}$ could be different for different cells. Thus, we use C_k^i and $W_{k,j}^i$ to

TABLE II. Accuracy test results of velocity component u for the porous plate problem.

Scheme	Mesh size	Quadrilateral Mesh		Triangular Mesh	
		L_1 errors	Order	L_1 errors	Order
HO	1/5	7.06×10^{-1}		1.014×10^{-1}	
	1/10	4.21×10^{-2}	4.068	6.82×10^{-3}	3.894
	1/20	3.35×10^{-3}	3.652	6.71×10^{-4}	3.346
	1/30	7.68×10^{-4}	3.629	1.86×10^{-4}	3.165
2O	1/10	1.09×10		3.07×10^{-1}	
	1/20	2.42×10^{-1}	2.174	7.72×10^{-2}	1.989
	1/30	1.04×10^{-1}	2.089	3.48×10^{-2}	1.969
	1/40	5.74×10^{-2}	2.057	1.99×10^{-2}	1.944

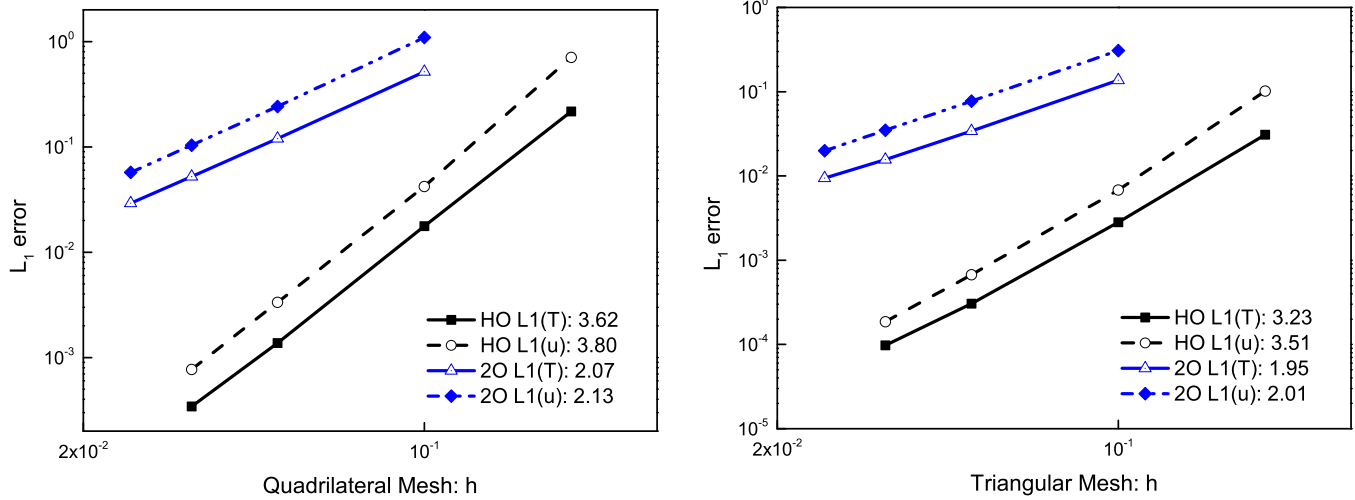


FIG. 3. Accuracy of the temperature T and velocity component u on quadrilateral mesh (left) and triangular mesh (right) at $Pr = 0.71$, $Re = 10$, and $Ra = 100$.

replace C_k and $W_{k,j}$ in Eq. (41) for the following derivations. With new notations, Eq. (41) reads

$$\int_{\Omega_i} \mathbf{U}(x, y) d\Omega = \left(\Omega_i - \sum_{k=1}^9 C_k^i \sum_{j=1}^N W_{k,j}^i \right) \mathbf{U}_i + \sum_{j=1}^N \left(\sum_{k=1}^9 C_k^i W_{k,j}^i \right) \mathbf{U}_{ij}. \quad (42)$$

If we substitute Eq. (42) into Eq. (7) and use variable \mathbf{R}_i to represent the flux contributions as given in Eq. (12) and the source term, then Eq. (7) can be written as

$$\left(\Omega_i - \sum_{k=1}^9 C_k^i \sum_{j=1}^N W_{k,j}^i \right) \frac{\partial \mathbf{U}_i}{\partial t} + \sum_{j=1}^N \left(\sum_{k=1}^9 C_k^i W_{k,j}^i \right) \frac{\partial \mathbf{U}_{ij}}{\partial t} = -\mathbf{R}_i. \quad (43)$$

As shown in Eq. (43), the time derivative terms consist of two parts: the solution value at the current cell i and those at the neighboring cells. To simplify the solution process, point iterative method is used to solve Eq. (43) efficiently. In fact, the following matrix form can be obtained when Eq. (43) is applied to all control cells:

$$\mathbf{M} \frac{\partial \mathbf{U}}{\partial t} = -\mathbf{R}, \quad (44)$$

where \mathbf{U} , \mathbf{R} is, respectively, the solution vector and the vector of flux and the source term contribution for all control cells; \mathbf{M} is a sparse matrix formed by coefficients on the left-hand side of Eq. (43).

When a steady state problem is considered, the time derivative in Eq. (44) is zero and the temporal accuracy is of no importance. Thus, we can use the first-order Euler explicit scheme to march Eq. (44) in time until a steady state solution

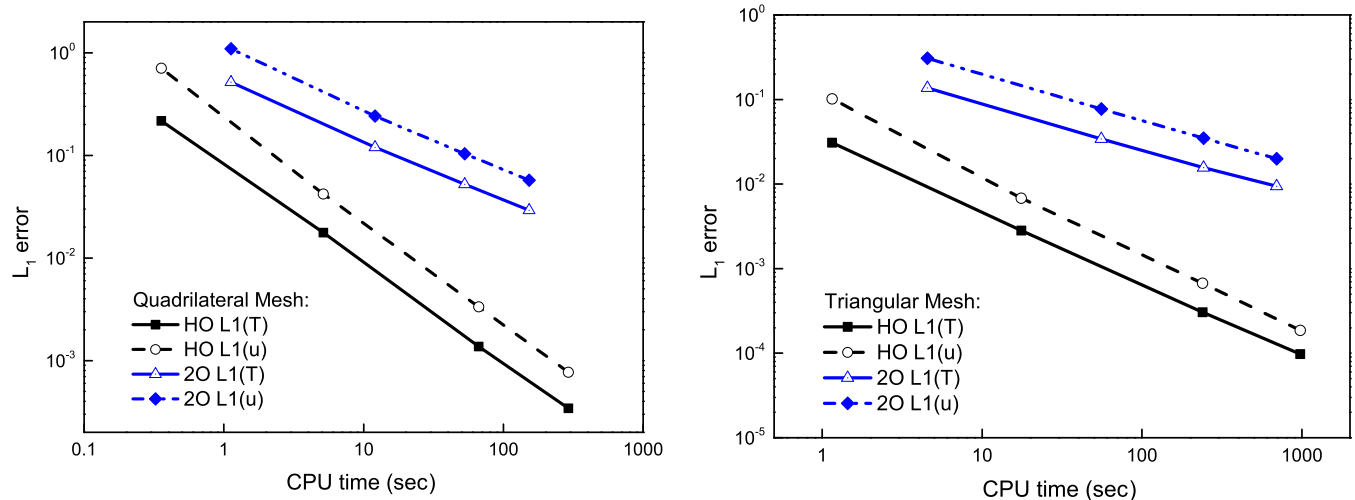


FIG. 4. Efficiency comparison between the HO and 2O LSFD-FV methods using TLBFS for porous plate problem on quadrilateral mesh (left) and triangular mesh (right) at $Pr = 0.71$, $Re = 10$, and $Ra = 100$.

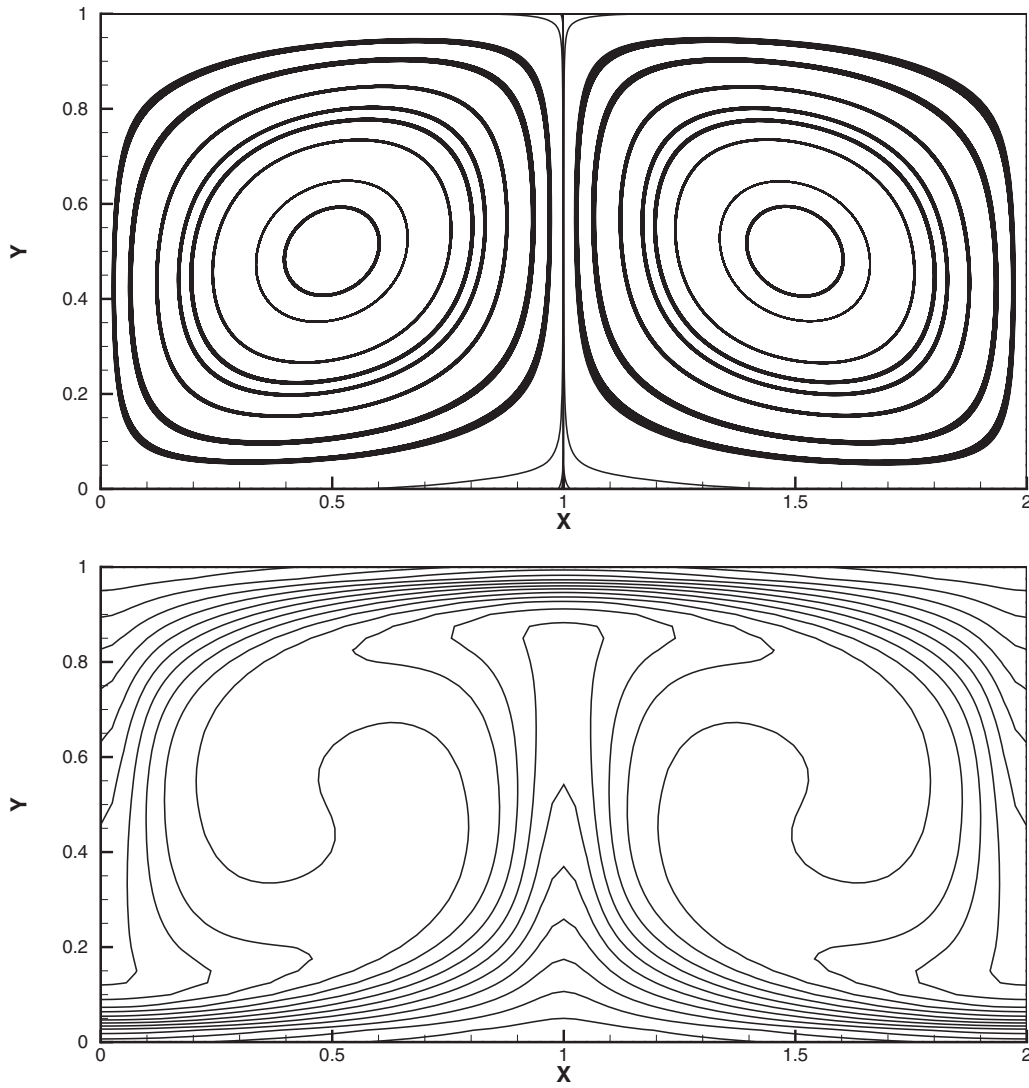


FIG. 5. Streamlines and isotherms for Rayleigh-Bénard convection problem by HO LSFD-FV method using TLBFS at Rayleigh number $Ra = 10^5$.

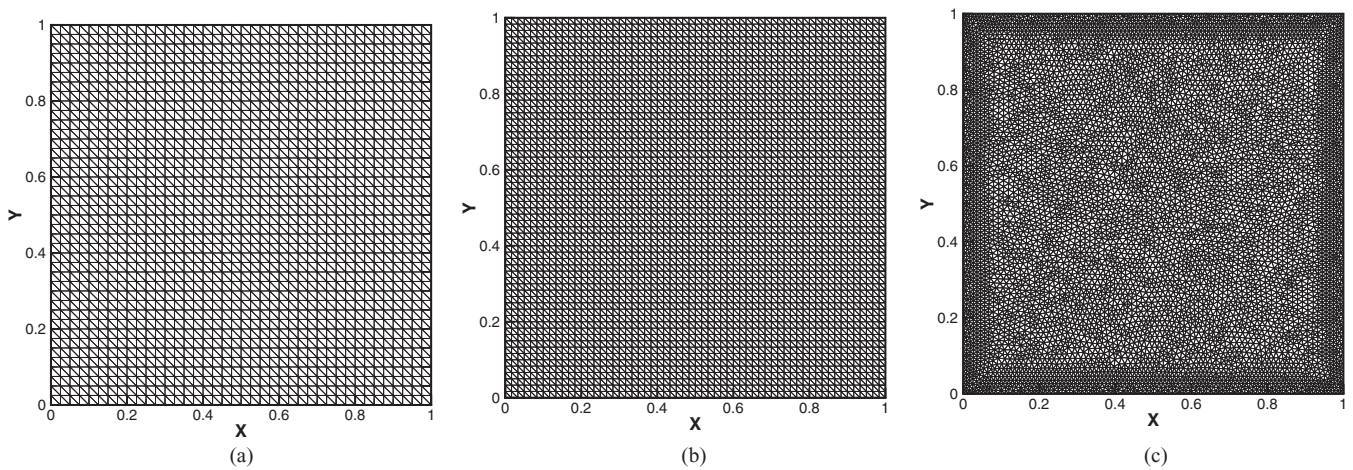


FIG. 6. Mesh used for natural convection in a square cavity by HO LSFD-FV method using TLBFS at different Rayleigh numbers: (a) $Ra = 10^3$, (b) $Ra = 10^4$, (c) $Ra = 10^5$, and 10^6 .

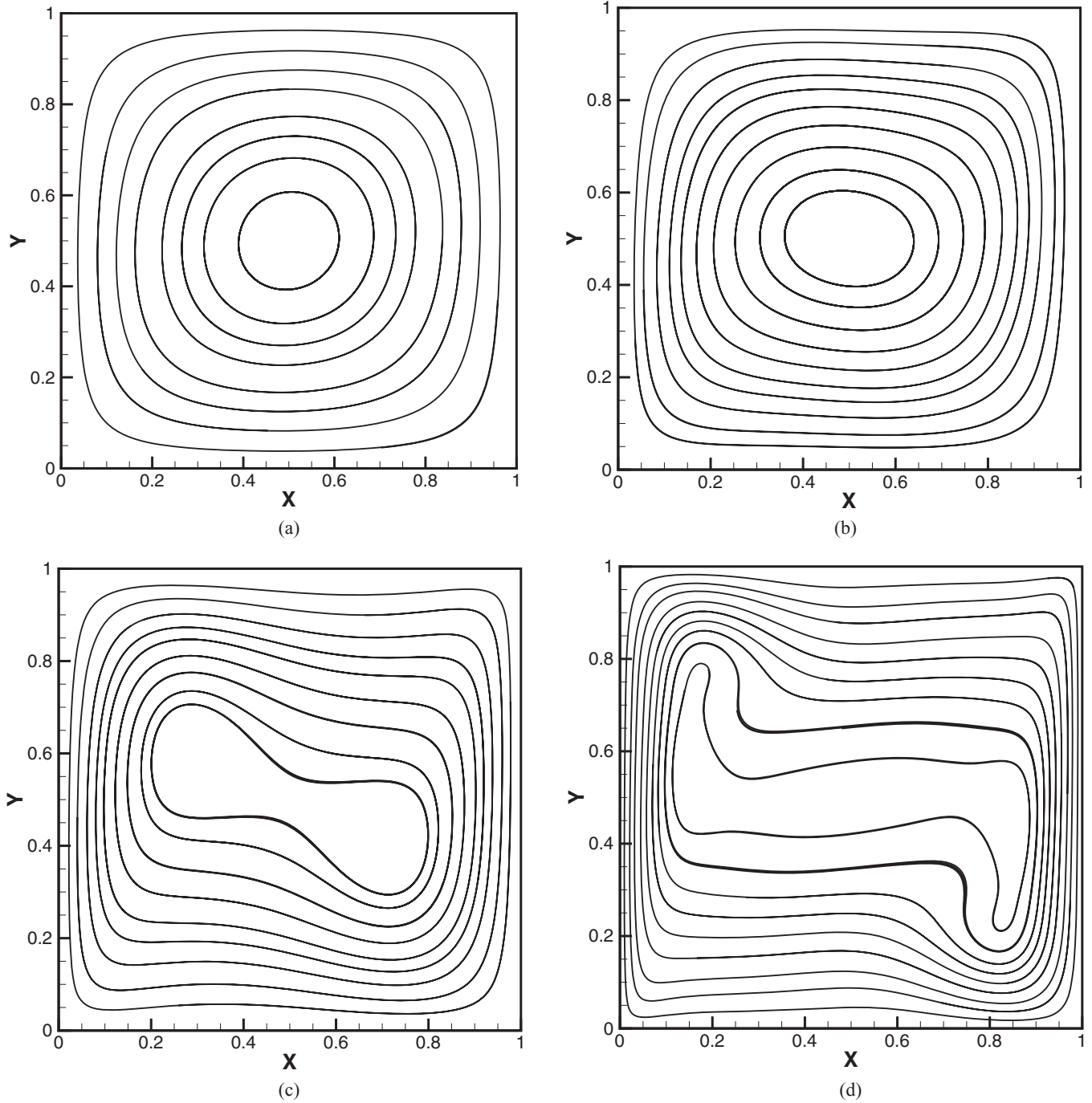


FIG. 7. Streamlines for natural convection in a square cavity by HO LSFD-FV method using TLBFS at different Rayleigh numbers: (a) $Ra = 10^3$, (b) $Ra = 10^4$, (c) $Ra = 10^5$, (d) $Ra = 10^6$.

is reached. Then Eq. (44) is written as

$$M \frac{U^{n+1} - U^n}{\Delta t} = -R^n. \tag{45}$$

If we use the point iterative method to solve Eq. (45), only at the current cell, U_i^{n+1} is written as

$$U_i^{n+1} = U_i^n + \Delta U_i^n. \tag{46}$$

For all the neighboring cells, U_{ij}^{n+1} is approximated by U_{ij}^n . As a consequence, Eq. (45) can be simplified to

$$M_{i,i} \frac{\Delta U_i^n}{\Delta t} = -R_i^n, \tag{47}$$

where $M_{i,i}$ are the diagonal elements and can be easily obtained from Eq. (43) as

$$M_{i,i} = \Omega_i - \sum_{k=1}^9 C_k^i \sum_{j=1}^N W_{k,j}^i. \tag{48}$$

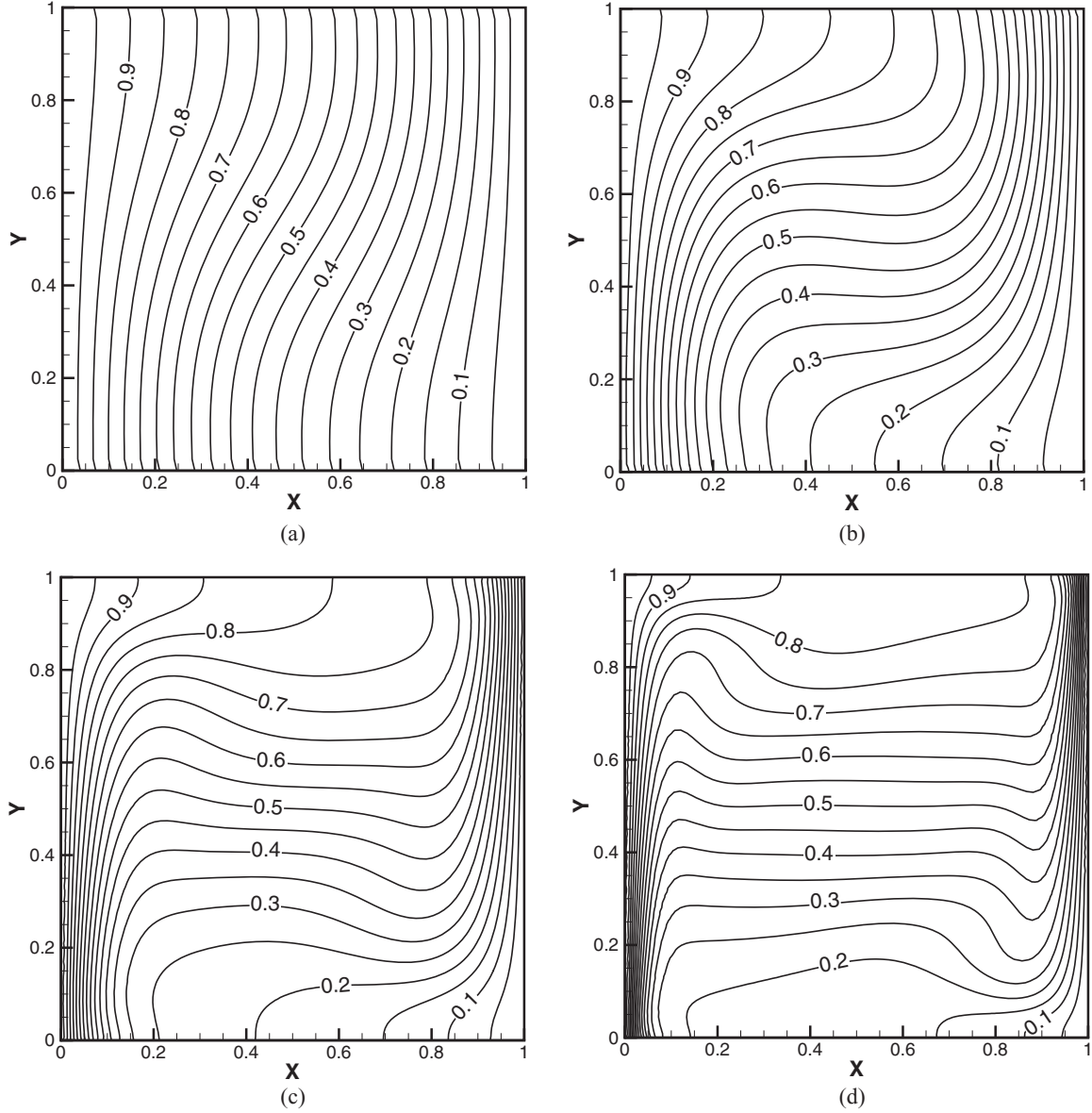


FIG. 8. Isotherms for natural convection in a square cavity by HO LSFD-FV method using TLBFS at different Rayleigh numbers: (a) $Ra = 10^3$, (b) $Ra = 10^4$, (c) $Ra = 10^5$, (d) $Ra = 10^6$.

As shown in Eq. (47), the solution for ΔU avoids the construction of matrix \mathbf{M} , which is usually hard to write out due to the unstructured distribution of mesh cells. Therefore, this simplified process is as convenient as the explicit method utilized in the conventional FV method. Once ΔU is obtained for all the control cells, the solution at the new time level ($n + 1$) can be updated by using Eq. (46).

For unsteady flow problems, the temporal accuracy is as important as the spatial accuracy. In Eq. (44), the time derivative is not zero and the sparse matrix \mathbf{M} affects the time evolution solution directly. In this case, in order to simplify the solution process in this work, the dual time stepping method [32] is adopted. By adding a pseudotime derivative to Eq. (44), we have

$$\mathbf{M} \frac{\partial U}{\partial \tau^*} + \mathbf{M} \frac{\partial U}{\partial t} = -\mathbf{R}, \quad (49)$$

where τ^* is the pseudotime. Introducing a new residual vector \mathbf{R}^* as

$$\mathbf{R}^* = \mathbf{R} + \mathbf{M} \frac{\partial U}{\partial t}, \quad (50)$$

then Eq. (49) can be reduced to

$$\mathbf{M} \frac{\partial U}{\partial \tau^*} = -\mathbf{R}^*. \quad (51)$$

As a result, Eq. (51) represents a steady state problem in the pseudotime domain. Thus, similar to the steady state case, the point iterative method described above can be used to solve Eq. (51). To ensure time accuracy, the matrix \mathbf{M} in \mathbf{R}^* cannot be simplified and the time derivative in \mathbf{R}^* is approximated by the 2O backward-difference scheme.

TABLE III. Results of natural convection in a square cavity at four different Rayleigh numbers: $Ra = 10^3, 10^4, 10^5$, and 10^6 .

		$Ra = 10^3$	$Ra = 10^4$	$Ra = 10^5$	$Ra = 10^6$
u_{\max}	Shu <i>et al.</i> [37]	3.649	16.190	34.736	64.775
	Yang <i>et al.</i> [35]	3.647	16.183	34.775	64.938
	Wang <i>et al.</i> [30]	3.640	16.14	34.87	64.838
	HO scheme	3.644	16.152	34.729	64.875
	2O scheme	3.622	16.150	34.791	65.011
y	Shu <i>et al.</i> [37]	0.815	0.825	0.855	0.850
	Yang <i>et al.</i> [35]	0.815	0.823	0.853	0.850
	Wang <i>et al.</i> [30]	0.815	0.825	0.855	0.850
	HO scheme	0.815	0.825	0.855	0.850
	2O scheme	0.824	0.816	0.854	0.851
v_{\max}	Shu <i>et al.</i> [37]	3.698	19.638	68.640	220.64
	Yang <i>et al.</i> [35]	3.696	19.627	68.634	220.67
	Wang <i>et al.</i> [30]	3.708	19.67	68.85	220.92
	HO scheme	3.693	19.612	68.355	218.34
	2O scheme	3.678	19.560	68.162	218.78
x	Shu <i>et al.</i> [37]	0.180	0.120	0.065	0.035
	Yang <i>et al.</i> [35]	0.175	0.117	0.067	0.038
	Wang <i>et al.</i> [30]	0.180	0.118	0.065	0.038
	HO scheme	0.176	0.117	0.067	0.035
	2O scheme	0.176	0.117	0.067	0.036
\overline{Nu}	Shu <i>et al.</i> [37]	1.118	2.245	4.523	8.762
	Yang <i>et al.</i> [35]	1.118	2.245	4.524	8.835
	Wang <i>et al.</i> [30]	1.115	2.232	4.491	8.711
	HO scheme	1.118	2.245	4.524	8.848
	2O scheme	1.119	2.254	4.535	8.936

III. NUMERICAL EXAMPLES

In this section, the accuracy of the developed HO LSFD-FV method is tested on triangular and quadrilateral grids first. Then the performance of this method is examined by a series of incompressible thermal flow problems. In order to further evaluate the robustness of HO LSFD-FV method, the challenging numerical examples involving heat transfer at very high Rayleigh numbers and/or with curved boundaries are also tested. In the simulation, for the present HO scheme, conservative variables at two sides of cell interface are interpolated by cubic approximation from those at cell centers. For comparison purposes, the 2O scheme using linear interpolation, which is the same as the work of Wang *et al.* [30], has been chosen as the basis to assess the capability of the present HO scheme.

A. Accuracy test with porous plate problem with a temperature gradient

For thermal incompressible flow simulations, the HO LSFD-FV method uses TLBFS to evaluate the inviscid and viscous fluxes simultaneously. In this work, the fourth-order accuracy interpolation is applied within every control cell. Thus, the conservation variables would be reconstructed with the fourth-order of accuracy and the LSFD-FV method itself can achieve the fourth-order of accuracy. This has been validated in the work of Liu *et al.* [28] by the accuracy test for the LSFD-FV method. However, the TLBFS only has

TABLE IV. Comparison of computational cost of HO and 2O LSFD-FV methods in natural convection in a square cavity at $Ra = 10^4$.

Methods	HO	2O	2O
Grids	7200	7200	28800
\overline{Nu}	2.245	2.254	2.247
Virtual memory (Megabytes)	24.8	12.0	29.5
Iteration steps	46999	50019	153747
Computational time (s)	4895.1	1377.9	17942.8

the 2O accuracy in solution reconstruction. Naturally, one may doubt the overall accuracy when these two methods are combined together. To clear up the doubts, we should note that the 2O accuracy of TLBFS is the local reconstruction accuracy in terms of δ_x or δ_t rather than the mesh spacing h . If δ_x is much smaller than h , the overall accuracy of the whole method which is assessed in terms of h will not be affected significantly by the TLBFS. Basically, there are some limitations for the choice of δ_x . In practical implementation, the present HO LSFD-FV method chooses two Gauss-Legendre quadrature points on every cell interface which can ensure the fourth-order accuracy of the surface integral. To avoid the extrapolation, the virtual streaming nodes should be inside the two control cells as depicted in Fig. 1. Thus, δ_x is restricted by the distribution of the Gauss-Legendre quadrature points and the control cell. Specifically, after numerous numerical studies, one effective and practical limitation for δ_x is that $\delta_x = (1/2 - \sqrt{3}/2)l_{\min} \sin \theta \approx 0.2113l_{\min} \sin \theta$, where l_{\min} and θ are the minimum length of the edge and the minimum interior angle among the left and right cells of the interface.

Based on the discussion above, the porous plate problem with a temperature gradient [33] is solved to conduct the convergence study for the HO LSFD-FV method with TLBFS. The physical configuration of this problem is a channel flow sheared between two porous plates, while an identical fluid is injected normal to the shearing direction from the bottom plate and withdrawn at the same rate from the upper plate. The steady state governing equations can be given as

$$v_0 \frac{\partial u}{\partial y} = v \frac{\partial^2 u}{\partial y^2},$$

$$\frac{\partial p}{\partial y} = g\beta(T - T_m), \quad (52)$$

$$v_0 \frac{\partial T}{\partial y} = \kappa \frac{\partial^2 T}{\partial y^2},$$

where v_0 is the injection velocity; T_h is the temperature for the bottom plate; T_c is the temperature for the upper plate, and $T_m = (T_h + T_c)/2$ is the average temperature. The steady state analytical solutions of the velocity component u and temperature T are given as

$$u = u_0 \left(\frac{e^{\text{Re} \cdot y/L} - 1}{e^{\text{Re}} - 1} \right), \quad (53)$$

$$T = T_c + \Delta T \left(\frac{e^{\text{Pr} \cdot \text{Re} \cdot y/L} - 1}{e^{\text{Pr} \cdot \text{Re}} - 1} \right), \quad (54)$$

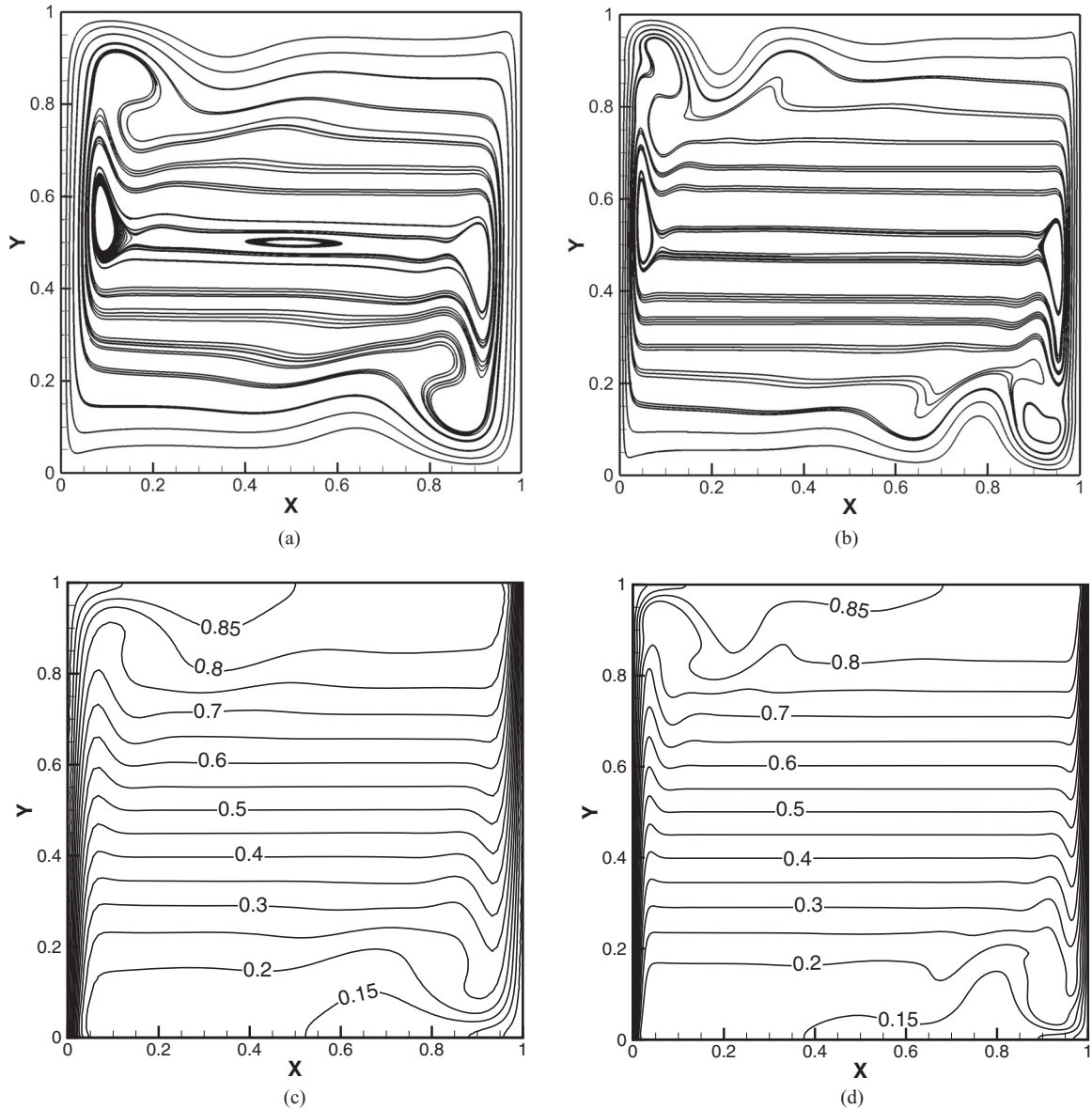


FIG. 9. Simulation results of HO LSFDFV method using TLBFS for natural convection in a square cavity. (a) Streamlines at $Ra = 10^7$, (b) streamlines at $Ra = 10^8$, (c) isotherms at $Ra = 10^7$, (d) isotherms at $Ra = 10^8$.

where u_0 is the velocity of the upper plate, Re is the Reynolds number, $\Delta T = T_h - T_c$ is the temperature difference between the upper and bottom plates, and $Pr = \nu/\kappa$ is the Prandtl number. This flow problem is also determined by the Rayleigh number which is defined by

$$Ra = \frac{g\beta\Delta TL^3}{\nu\kappa}. \quad (55)$$

The computation is on a square domain $[-L, L] \times [-L, L]$ at $Re = v_0L/\nu = 10$, $Pr = 0.71$ and $Ra = 100$. The relaxation parameter τ_v is set as 0.8 and the streaming distance δ_x is selected as $0.2l_{\min} \sin\theta$. Periodic boundary condition is imposed at the entrance and exit of the channel and the Dirichlet boundary conditions are used at the top and bottom plates.

Figure 2 plots the velocity and temperature profiles obtained by the present HO LSFDFV method, i.e. the HO

scheme, and the analytical solutions on the quadrilateral mesh with the mesh size $h = 1/30$. It is clear that the results of the HO scheme have good agreement with the analytical solutions. This indicates that the present HO method using TLBFS can capture the distribution of the velocity and temperature in the flow field accurately. For the convergence study, the accuracy of the 2O scheme is tested as a validation and comparison. In the test, four regular quadrilateral and triangular grids with the mesh size of $h = 1/10, 1/20, 1/30$, and $1/40$ are used. The accuracy of the HO scheme is examined on the grids of $h = 1/5, 1/10, 1/20$, and $1/30$. Table I lists errors of temperature T in terms of L_1 norm and the convergence rates on the quadrilateral and triangular grids, respectively. In Table II, accuracy test results of the velocity component u are shown. Evidently, the relative errors of the HO scheme are much smaller than the 2O scheme, which reflects the higher order accuracy of the HO scheme. The slopes of

TABLE V. Results of natural convection in a square cavity at $Ra = 10^7$ and 10^8 .

Ra		10^7	10^8
Nu_0	Chen <i>et al.</i> [20]	16.558	30.37
	Quéré [39]	16.523	30.23
	Mayne <i>et al.</i> [40]	16.387	29.63
	HO scheme	16.685	30.064
	2O scheme	17.187	30.966
u_{\max}	Chen <i>et al.</i> [20]	148.81	324.22
	Quéré [39]	148.59	321.9
	Mayne <i>et al.</i> [40]	145.27	283.07
	HO scheme	148.83	324.05
	2O scheme	151.76	264.85
v_{\max}	Chen <i>et al.</i> [20]	699.52	2221.3
	Quéré [39]	699.18	2222
	Mayne <i>et al.</i> [40]	703.25	2223.4
	HO scheme	698.58	2202.7
	2O scheme	690.37	2247.5

linearly fitted lines in Fig. 3 reveal that the accuracy of both schemes can achieve the designed order and the HO LSFD-FV method can achieve more than three roughly for both velocity and temperature field, which is consistent with the above discussion of accuracy. Furthermore, Fig. 4 compares the efficiency between the HO and 2O schemes. It is shown that the HO scheme with TLBFS requires less CPU time than the 2O one to achieve the same accuracy. This provides evident proof for the better efficiency of the HO LSFD-FV method.

B. Rayleigh-Bénard convection

Rayleigh-Bénard convection, as a classic benchmark case of natural convection, is simulated to test the developed HO method. This problem models a viscous fluid between two horizontal walls which is heated from the bottom and cooled by the top. The temperatures at the bottom and top walls are

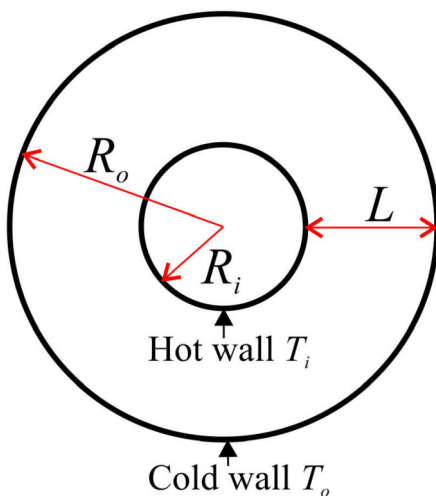


FIG. 10. Illustration of the setup for natural convection in a concentric annulus.

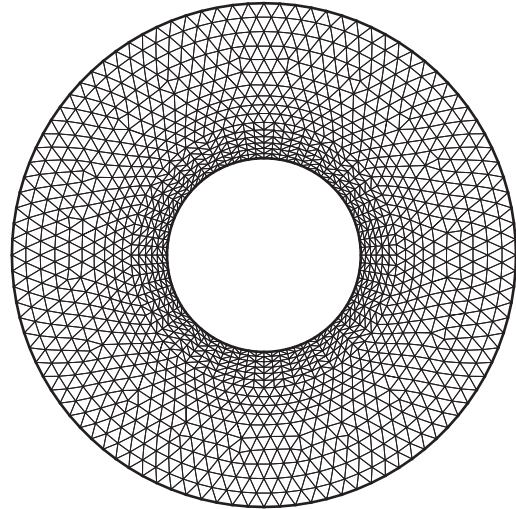


FIG. 11. Mesh used for natural convection in a concentric annulus at different Rayleigh numbers. Control cells: 2740.

$T_1 = 1$ and $T_0 = 0$, respectively, with the difference $\Delta T = 1$. The dynamic similarity of this case is determined by the dimensionless parameters of Prandtl number Pr and Rayleigh number Ra . In the present simulation, the Rayleigh number Ra is defined as below using the vertical length scale H as the characteristic length:

$$Ra = \frac{g\beta\Delta TH^3}{\nu\kappa} = \frac{V_c^2 H^2}{\nu\kappa}, \quad (56)$$

where $V_c = \sqrt{g\beta H \cdot \Delta T}$ is the characteristic thermal velocity constrained by the low Mach number limit. For this test case, we set $Pr = 0.71$, $V_c = 0.1$, and $Ra = 10^5$. The horizontal and vertical length scales are, respectively, chosen as $L = 2$ and $H = 1$. No-slip boundary conditions are applied on the bottom and top walls, and periodic boundary conditions are implemented at the left and right boundaries. The computational domain is divided by 3200 regular quadrilateral cells. The computed streamlines and isotherms by the present HO LSFD-FV method using TLBFS are shown in Fig. 5. It can be observed that the heat transfer in the box can be captured accurately and these results agree well with the literature [34,35]. The agreements validate the present HO LSFD-FV method using TLBFS.

C. Natural convection in a square cavity

The following benchmark case is the natural convection in a square cavity, driven by the buoyancy force. It is a good test problem for validating new numerical methods at a wide range of Rayleigh numbers, and it has been used for many previous studies [20,30,35,36]. In our simulation, the no-slip boundary condition is applied on all walls. The adiabatic condition is set on the top and bottom walls, while isothermal conditions with fixed temperatures of $T_1 = 1$ and $T_0 = 0$ are implemented at the left and right walls, respectively. The dynamic similarity of this problem is determined by the Prandtl number Pr and the Rayleigh number Ra which is defined the same as Eq. (55). Here, we set $L = 1$, $Pr = 0.71$ and $V_c = 0.1$. Commonly, the Nusselt number Nu is used to evaluate the heat transfer rate.

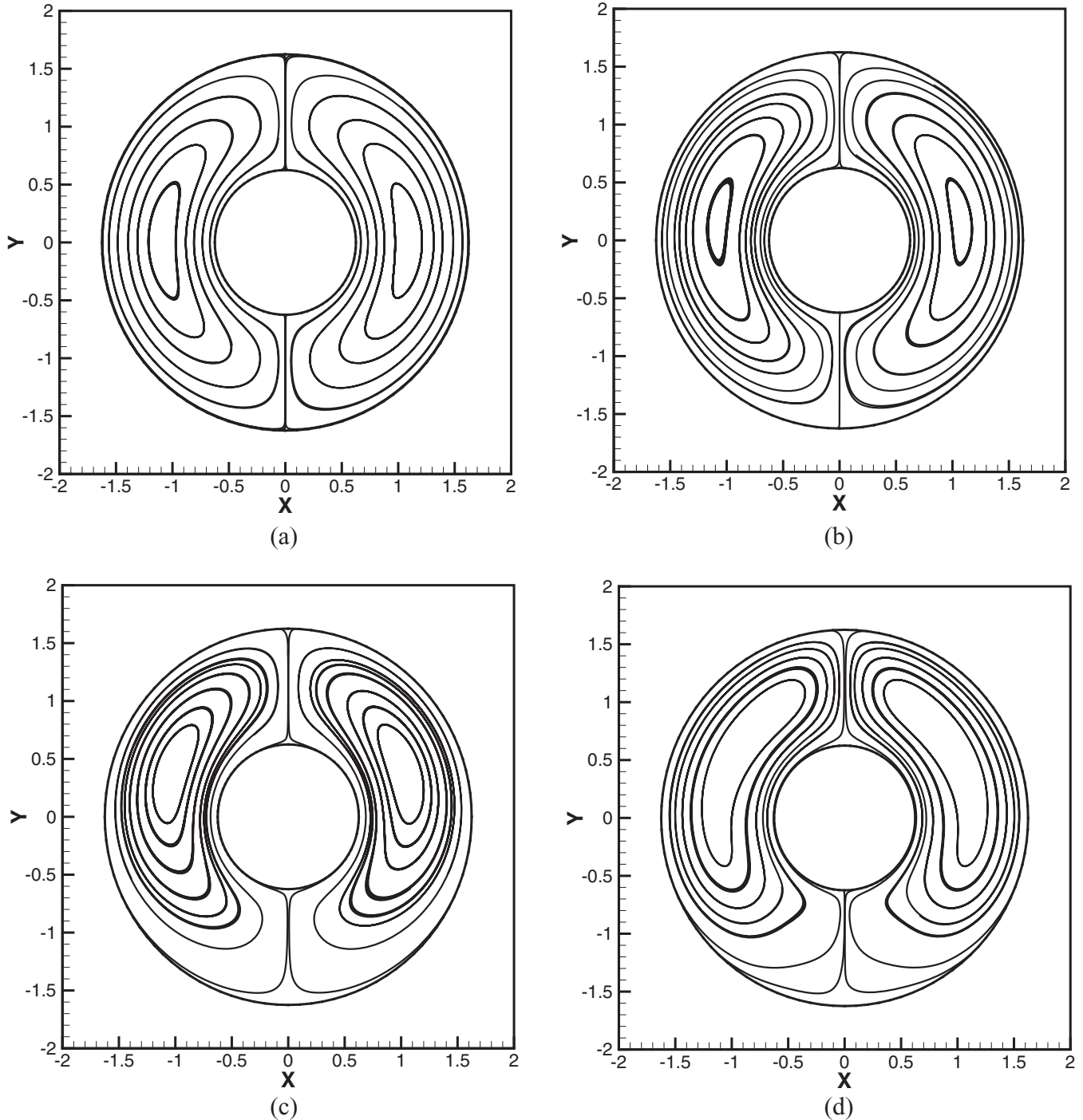


FIG. 12. Streamlines for natural convection in a concentric annulus by HO LSFD-FV method using TLBFS at different Rayleigh numbers: (a) $Ra = 10^2$, (b) $Ra = 10^3$, (c) $Ra = 10^4$, (d) $Ra = 5 \times 10^4$.

The averaged Nusselt number over the whole flow domain and that along the vertical boundary of $x = 0$ are, respectively, defined as

$$\overline{Nu} = \frac{L}{\kappa \Delta T L^2} \iint_{\Omega} \left(uT - \kappa \frac{\partial T}{\partial x} \right) d\Omega, \quad (57)$$

$$Nu_0 = \frac{L}{\Delta T L} \int_{x=0} \frac{\partial T}{\partial x} dy. \quad (58)$$

First, a series of tests at $Ra = 10^3$, 10^4 , 10^5 , and 10^6 are carried out on three different unstructured grids with 3200, 7200, and 14 554 cells, respectively, as shown in Fig. 6. For the case of $Ra = 10^3$ and 10^4 , the grids with 3200 and 7200 cells are employed, respectively. For $Ra = 10^5$ and 10^6 , the refined grids with 14554 cells are used. Figures 7 and 8 depict the streamlines and isotherms computed by the present HO method, respectively. These results have good agreement with those obtained by Peng *et al.* [36], Wang *et al.* [30], and Chen

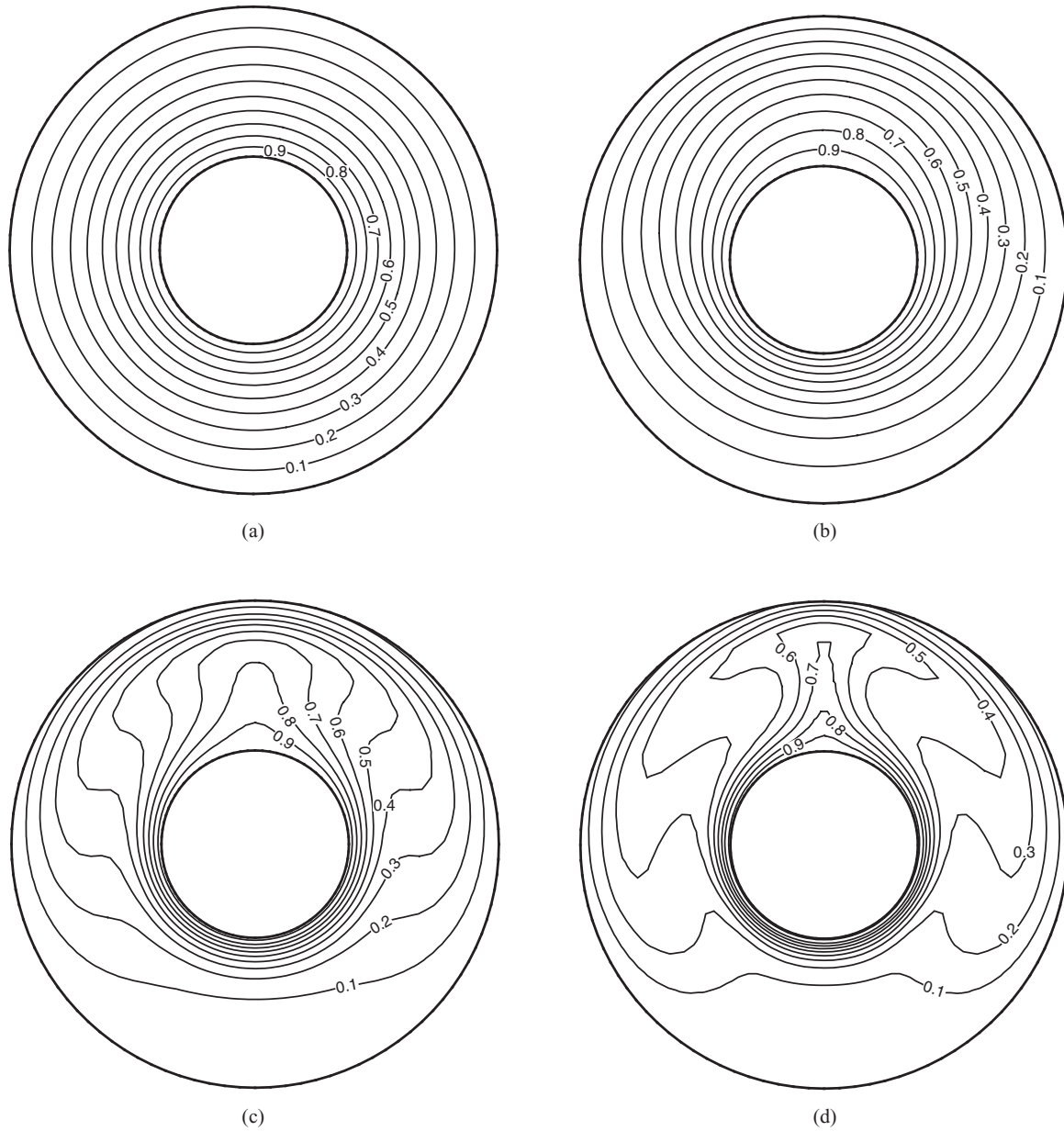


FIG. 13. Isotherms for natural convection in a concentric annulus by HO LSFDFV method using TLBFS at different Rayleigh numbers: (a) $Ra = 10^2$, (b) $Ra = 10^3$, (c) $Ra = 10^4$, (d) $Ra = 5 \times 10^4$.

et al. [20]. Additionally, Table III quantitatively compares the computed representative properties, i.e., the average Nusselt number \overline{Nu} , the maximum velocity u at the vertical centerline u_{max} , the maximum velocity v at the horizontal centerline v_{max} and their corresponding locations, with those of Wang

et al. [30], Yang *et al.* [35], and Shu and Xue [37]. We can see that results obtained by the HO scheme agree well with those reported in literature. Moreover, it is noteworthy that the previous work [30,35] used a much more refined mesh to get the ideal results while relatively coarse grids are used in the

TABLE VI. Comparison of average equivalent heat conductivity for natural convection in a concentric annulus at different Rayleigh numbers.

Ra	Inner cylinder, $\overline{k_{eqi}}$				Outer cylinder, $\overline{k_{eqo}}$			
	Kuehn <i>et al.</i> [42]	Shu <i>et al.</i> [41]	HO scheme	2O scheme	Kuehn <i>et al.</i> [42]	Shu <i>et al.</i> [41]	HO scheme	2O scheme
10^2	1.000	1.001	1.001	1.000	1.002	1.001	1.001	1.000
10^3	1.081	1.082	1.084	1.089	1.084	1.082	1.084	1.089
10^4	2.010	1.979	2.001	2.044	2.005	1.979	2.000	2.043
5×10^4	3.024	2.958	3.015	3.104	2.973	2.958	3.013	3.102

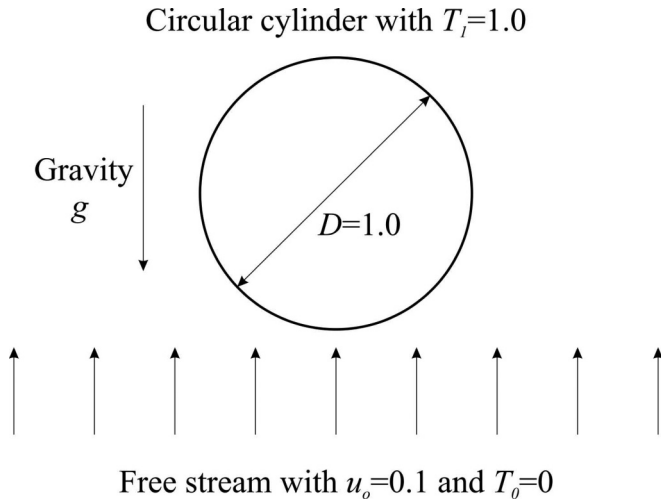


FIG. 14. Illustration of the mixed heat transfer simulation setup from a heated circular cylinder.

present work, which reflects the higher accuracy of the present HO scheme. This can be proven again from the comparison between the results of HO scheme and the 2O scheme on the same mesh in Table III.

Apart from the accuracy, the computational efficiency and memory cost of the HO LSFD-FV method are tested and compared with the 2O one. Here, we choose the case of $Ra = 10^4$ as an example and the corresponding results are presented in Table IV. As can be seen, although both the memory cost and computational time of the HO scheme are higher than the 2O scheme on the same mesh with 7200 triangular cells, the results of the 2O scheme do not accord with those in the literature. When the refined mesh with 28 800 triangular cells is used for the 2O scheme to get the comparable results as the HO scheme, the memory cost of the HO scheme only accounts for 84% of that of the 2O scheme, while the computational time of the HO scheme is as little as 27% of that of the 2O scheme. This provides evident proof

for the better computational efficiency of the HO LSFD-FV method.

Finally, two more challenging cases of $Ra = 10^7$ and 10^8 are solved on the unstructured mesh which has 100 grid points at each boundary, totally 14 554 cells, as shown in Fig. 6. Figure 9 presents the computed streamlines and isotherms. It can be seen that, in comparison with the case at moderate Rayleigh numbers ($Ra = 10^3, 10^4, 10^5$, and 10^6), both the flow and temperature boundary layers close to the hot and cold walls at $Ra = 10^7$ and 10^8 are very thin. Moreover, vertical convection in the central area becomes very weak and heat conduction dominates this region. These observations keep in accordance with results in Refs. [35,38]. Detailed comparisons of representative quantities of Nu_0 , u_{\max} and v_{\max} are presented in Table V. From these results, it can be concluded that the HO LSFD-FV method using TLBFS can capture highly squeezed isotherms and streamlines on coarse unstructured meshes and the HO LSFD-FV scheme is more accurate than the 2O one.

D. Natural convection in a concentric annulus

The previous three test cases have validated the present HO LSFD-FV method using TLBFS for simulation of thermal flow problems with relatively simple geometry. To further illustrate the flexibility and capability of the present method in the use of unstructured mesh for solving thermal problems with curved boundaries, a numerical test of the natural convection in a concentric annulus [30,35,41,42] is presented in this subsection. A schematic diagram of the problem is shown in Fig. 10. From this figure, the temperature of the hot inner cylinder with radius R_i is $T_i = 1$ and that of the cold outer cylinder with radius R_o is $T_o = 0$. The distance L between these two cylinders is selected as the characteristic length. The dynamic similarity of this problem depends on three dimensionless parameters, i.e., the aspect ratio A_r , Pr , and Ra . Pr and Ra were previously defined while the aspect

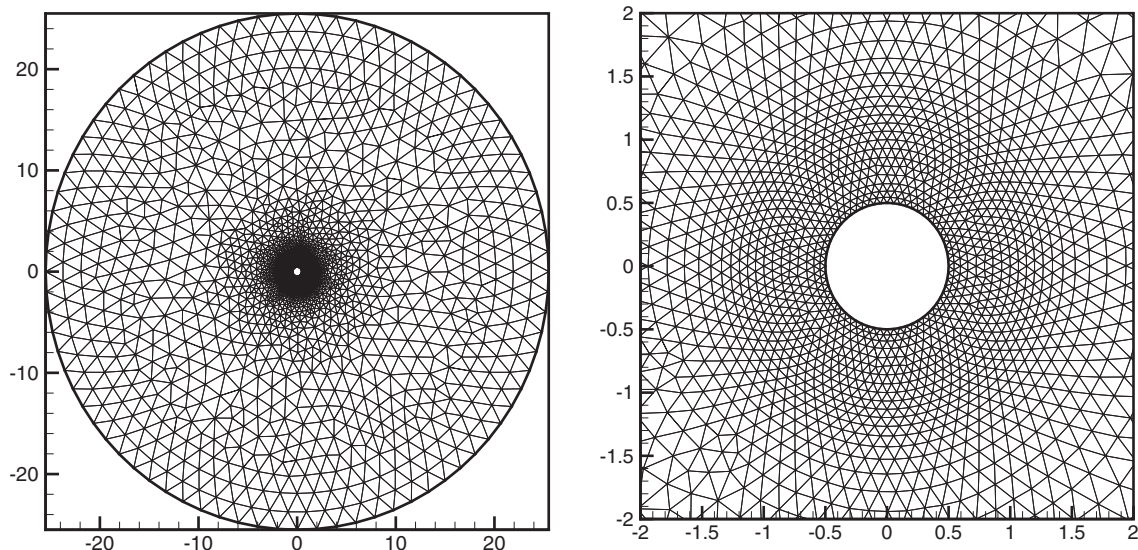


FIG. 15. Mesh used for mixed heat transfer from a heated circular cylinder at various Grashof numbers. Control cells: 5600.

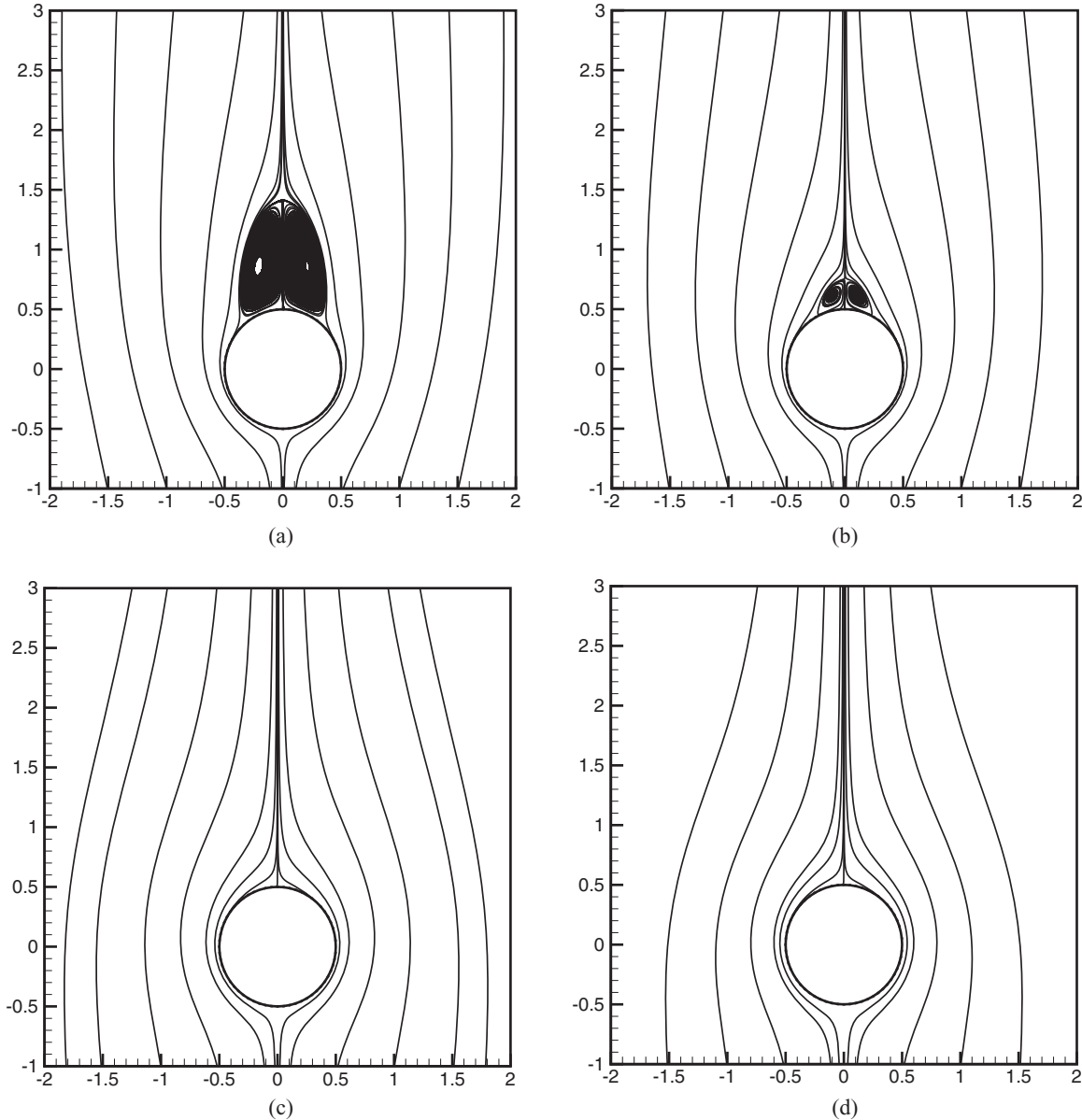


FIG. 16. Streamlines for mixed convection obtained by HO LSFD-FV method using TLBFS at $Re = 20$ and various Gr : (a) $Gr = 0$, (b) $Gr = 100$, (c) $Gr = 800$, (d) $Gr = 1600$.

ratio A_r is defined as

$$A_r = \frac{R_o}{R_i}. \quad (59)$$

Moreover, the average equivalent heat conductivities on the inner and outer cylinders are defined as follows to quantify the heat transfer efficiency of this problem:

$$\overline{k_{eqi}} = \frac{\ln(A_r)}{2\pi(A_r - 1)} \int_0^{2\pi} \frac{\partial T}{\partial r} d\theta, \quad (60)$$

$$\overline{k_{eqo}} = \frac{A_r \ln(A_r)}{2\pi(A_r - 1)} \int_0^{2\pi} \frac{\partial T}{\partial r} d\theta. \quad (61)$$

In the simulation, A_r is set as 2.6 and $Pr = 0.71$. Four cases at various Rayleigh numbers of $Ra = 10^3$, 10^4 , and 5×10^4 are carried out on the unstructured mesh with 2740 triangular cells as shown in Fig. 11. Figures 12 and 13 present the streamlines and isotherms at different Rayleigh numbers

obtained by the HO LSFD-FV method using TLBFS, respectively. It can be seen that at lower Rayleigh number, e.g., $Ra = 10^2$, both isotherms and streamlines are nearly symmetric about the x and y axes. This phenomenon indicates that, when Rayleigh number is low, the thermal conduction dominates the heat transfer. Thus, the heat transfer efficiency is relatively low. With Rayleigh number increased, the rotational centers of the flow field move upwards and the thermal boundary layers of both inner and outer cylinders separate gradually. This means that, when Rayleigh number exceeds 10^3 , thermal convection becomes strong enough to affect the thermal field and the heat transfer efficiency is increased. These observations can be quantitatively verified via the equivalent conductivities in Table VI. Besides the converged results obtained by the present HO method, results of the 2O counterpart and the data given by Shu [41], Kuehn and Goldstein [42] are included for comparison. As the discussion above, the equivalent

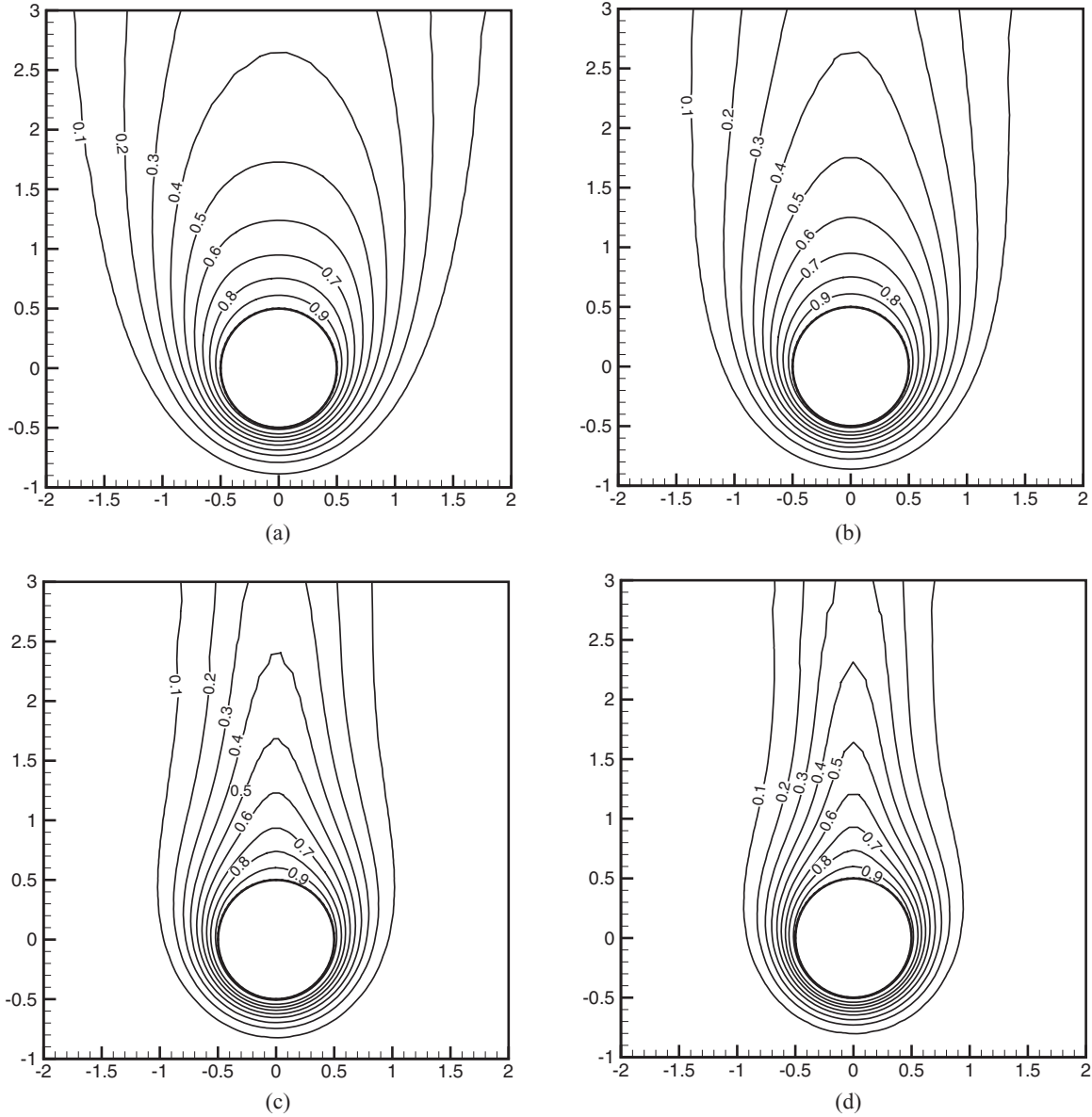


FIG. 17. Isotherms for mixed convection obtained by HO LSFD-FV method using TLBFS at $Re = 20$ and various Gr : (a) $Gr = 0$, (b) $Gr = 100$, (c) $Gr = 800$, (d) $Gr = 1600$.

conductivities on both inner and outer cylinders increase gradually when the Rayleigh number becomes larger. From Table VI, it can be observed that the computed parameters by the present HO scheme agree well with the reference data and the maximum relative error between the present results and the benchmark data is within 2%. Furthermore, through the comparison between the HO scheme and the 2O scheme in Table VI, it is clear that the HO method outperforms the 2O one in terms of the accuracy.

E. Mixed heat transfer from a heated circular cylinder

To further demonstrate the capability of the present HO LSFD-FV method using TLBFS for solving thermal flow problems with curved boundary, validation on the mixed heat transfer from a heated circular cylinder is conducted at Reynolds number $Re = 20$ and various Grashof number

$Gr = 0, 100, 800, \text{ and } 1600$. Physically, as illustrated in Fig. 14, both natural heat convection and forced heat convection are involved in this problem. Therefore, this test case is more complicated than the previous examples. Apart from the Prandtl number defined previously with the characteristic length D , the Reynolds number Re , Grashof number Gr , and average Nusselt number \bar{Nu} are usually introduced for better description of the mixed convection problem. These nondimensional parameters are defined as follows:

$$Re = \frac{u_0 D}{\nu}, \tag{62}$$

$$Gr = \frac{g\beta(T_1 - T_0)D^3}{\nu^2}, \tag{63}$$

$$\bar{Nu} = \frac{D}{2\pi(T_1 - T_0)} \int_0^{2\pi} \frac{\partial T}{\partial n} d\theta. \tag{64}$$

TABLE VII. Comparison of average Nusselt number and separation angle on a circular cylinder for mixed convection at $Re = 20$ and various Gr .

Gr	\overline{Nu}			$\theta_s(\text{deg})$		
	Badr <i>et al.</i> [43]	Yang <i>et al.</i> [35]	HO scheme	Badr <i>et al.</i> [43]	Yang <i>et al.</i> [35]	HO scheme
0	2.540	2.454	2.454	43.13	43.59	43.57
100	2.654	2.655	2.662	29.51	30.01	29.60
800	3.227	3.201	3.210	0.0	0.0	0.0
1600	3.564	3.508	3.524	0.0	0.0	0.0

In the present simulation, $Pr = 0.7$, $u_0 = 0.1$, $T_1 = 1$, and $T_0 = 0$ are chosen to accord with the initial setup in Refs. [30,43]. The computation is on the unstructured mesh which has 5600 triangular cells as shown in Fig. 15. The far-field boundary is set at 25.5 diameters away from the center of the cylinder.

Figures 16 and 17, respectively, plot the computed streamlines and isotherms at four different Grashof numbers by the present HO method. When $Gr = 0$, the temperature field has no effect on the flow field. Hence, the streamlines obtained are the same as those in isothermal simulations at the same Reynolds number and clear recirculation zones are captured. With the increase of Grashof number, the separation angle θ_s and the length of the vortex behind the circular cylinder decrease gradually until the vortex disappears at $Gr \geq 800$. This indicates that the heat transfer rate may increase and the viscous effect becomes weaker as Gr increases, which can be verified via the isotherm figure. Table VII lists the quantitative comparison between the computed average Nusselt number \overline{Nu} and separation angle θ_s on the circular cylinder with the results of Badr [43] and Yang *et al.* [35]. As can be seen, as Gr is increased, \overline{Nu} increases but θ_s decreases, which keeps in accordance with trends in the streamlines and isotherms shown in Figs. 16 and 17. Meanwhile, good agreements between the results of the present HO method and the published data [35,43] can be achieved. These validate the accuracy and the flexibility on unstructured grids of the present HO LSFD-FV method with TLBFS for solving the complicated heat transfer flow problem with curved boundaries.

IV. CONCLUSIONS

This paper presents a straightforward HO least-square-based finite difference-finite volume method on arbitrary grids for simulation of incompressible thermal flows. This HO method is based on the polynomial approximation with a high order Taylor series expansion, where unknown derivatives are approximated by the mesh-free LSFD technique. Different from the other HO FV methods, the LSFD-FV method directly uses the Taylor series expansion as the approximation function within the control cell. This provides the present method with the advantage of a straightforward algorithm and easy comprehension. Moreover, this highly accurate LSFD-FV method adopts TLBFS to evaluate the inviscid and viscous fluxes simultaneously without introducing new degrees of freedom, which makes the HO LSFD-FV method competitive in terms of the viscous discretization.

Representative simulations validate the robustness, accuracy, and computational efficiency of the present HO method as well as its capability of handling the problems with a curved boundary on unstructured grids. Numerical results show that the HO LSFD-FV method can achieve the third order of accuracy. Furthermore, compared with the 2O scheme, the HO method can obtain more precise results with less computational cost. Such outcomes indicate that the HO LSFD-FV method with TLBFS has great potential in simulating practical heat transfer problems.

- [1] M. N. Özişik, H. R. Orlande, M. J. Colaço, and R. M. Cotta, *Finite Difference Methods in Heat Transfer* (CRC, Boca Raton, FL, 2017).
- [2] M. Zeng, P. Yu, F. Xu, and Q. W. Wang, Natural convection in triangular attics filled with porous medium heated from below, *Numer. Heat Transfer A*, **63**, 735 (2013).
- [3] Z. Guo, C. Zheng, B. Shi, and T. S. Zhao, Thermal lattice Boltzmann equation for low Mach number flows: Decoupling model, *Phys. Rev. E* **75**, 036704 (2007).
- [4] A. Çıbık and S. Kaya, A projection-based stabilized finite element method for steady-state natural convection problem, *J. Math. Anal. Appl.* **381**, 469 (2011).
- [5] Y. Cao and Y. Zhang, Investigation on the natural convection in horizontal concentric annulus using the variable property-based lattice Boltzmann flux solver, *Int. J. Heat Mass Transfer* **111**, 1260 (2017).
- [6] H. N. Dixit and V. Babu, Simulation of high Rayleigh number natural convection in a square cavity using the lattice Boltzmann method, *Int. J. Heat Mass Transfer* **49**, 727 (2006).
- [7] Z. Chen, C. Shu, and D. Tan, A simplified thermal lattice Boltzmann method without evolution of distribution functions, *Int. J. Heat Mass Transfer* **105**, 741 (2017).
- [8] A. Mohebbi and M. Dehghan, High-order compact solution of the one-dimensional heat and advection-diffusion equations, *Appl. Math. Model.* **34**, 3071 (2010).
- [9] Z. F. Tian and Y. B. Ge, A fourth-order compact finite difference scheme for the steady stream function-vorticity formulation of the Navier-Stokes/Boussinesq equations, *Int. J. Numer. Methods Fluids* **41**, 495 (2003).

- [10] J. Zhao, W. Dai, and T. Niu, Fourth-order compact schemes of a heat conduction problem with Neumann boundary conditions, *Numer. Methods Partial Differ. Equ.* **23**, 949 (2007).
- [11] M. Sari, G. Gürarşlan, and A. Zeytinoglu, High-order finite difference schemes for solving the advection-diffusion equation, *Math. Comput. Appl.* **15**, 449 (2010).
- [12] B. X. Zhao and Z. F. Tian, High-resolution high-order upwind compact scheme-based numerical computation of natural convection flows in a square cavity, *Int. J. Heat Mass Transf.* **98**, 313 (2016).
- [13] M. Xu, A type of high order schemes for steady convection-diffusion problems, *Int. J. Heat Mass Transf.* **107**, 1044 (2017).
- [14] Y. Zhao and B. Zhang, A high-order characteristics upwind FV method for incompressible flow and heat transfer simulation on unstructured grids, *Comput. Meth. Appl. Mech. Eng.* **190**, 733 (2000).
- [15] W. H. Wu and X. K. Li, Application of the time discontinuous Galerkin finite element method to heat wave simulation, *Int. J. Heat Mass Transf.* **49**, 1679 (2006).
- [16] Z. R. Hao, C. W. Gu, and X. D. Ren, The application of discontinuous Galerkin methods in conjugate heat transfer simulations of gas turbines, *Energies* **7**, 7857 (2014).
- [17] Z. Cai and B. Thornber, An internal penalty discontinuous Galerkin method for simulating conjugate heat transfer in a closed cavity, *Int. J. Numer. Methods Fluids* **87**, 134 (2018).
- [18] D. Liu, X. Zheng, and Y. Liu, A discontinuous Galerkin finite element method for heat conduction problems with local high gradient and thermal contact resistance, *CMES: Comp. Model. Eng.* **39**, 263 (2009).
- [19] S. R. G. Polasanapalli and K. Anupindi, A high-order compact finite-difference lattice Boltzmann method for simulation of natural convection, *Comput. Fluids* **181**, 259 (2019).
- [20] Z. Chen, C. Shu, and D. Tan, High-order simplified thermal lattice Boltzmann method for incompressible thermal flows, *Int. J. Heat Mass Transf.* **127**, 1 (2018).
- [21] A. Rouboa and E. Monteiro, Heat transfer in multi-block grid during solidification: Performance of finite differences and finite volume methods, *J. Mater. Process. Technol.* **204**, 451 (2008).
- [22] M. Goodarzi, M. R. Safaei, A. Karimipour, K. Hooman, M. Dahari, S. N. Kazi, and E. Sadeghinezhad, Comparison of the finite volume and lattice Boltzmann methods for solving natural convection heat transfer problems inside cavities and enclosures, *Abstr. Appl. Anal.* **2014**, 762184 (2014).
- [23] H. Ding, C. Shu, and K. S. Yeo, Development of least square-based two-dimensional finite difference schemes and their application to simulate natural convection in a cavity, *Comput. Fluids* **33**, 137 (2004).
- [24] H. Ding, C. Shu, K. S. Yeo, and D. Xu, Simulation of incompressible viscous flows past a circular cylinder by hybrid FD scheme and meshless least square-based finite difference method, *Comput. Methods Appl. Mech. Eng.* **193**, 727 (2004).
- [25] C. Shu, W. X. Wu, H. Ding, and C. M. Wang, Free vibration analysis of plates using least-square-based finite difference method, *Comput. Methods Appl. Mech. Eng.* **196**, 1330 (2007).
- [26] H. Ding, C. Shu, K. S. Yeo, and D. Xu, Numerical simulation of flows around two circular cylinders by mesh-free least square-based finite difference methods, *Int. J. Numer. Meth. Fluids* **53**, 305 (2007).
- [27] W. X. Wu, C. Shu, and C. M. Wang, Mesh-free least-squares-based finite difference method for large-amplitude free vibration analysis of arbitrarily shaped thin plates, *J. Sound Vib.* **317**, 955 (2008).
- [28] Y. Y. Liu, C. Shu, H. W. Zhang, and L. M. Yang, A high order least square-based finite difference-finite volume method with lattice Boltzmann flux solver for simulation of incompressible flows on unstructured grids, *J. Comput. Phys.* **401**, 109019 (2020).
- [29] T. J. Barth and P. O. Frederickson, Higher order solution of the Euler equations on unstructured grids using quadratic reconstruction, in *AIAA, 28th Aerospace Sciences Meeting, Reno, NV, 1990* (AIAA, Reno, 1990).
- [30] Y. Wang, C. Shu, and C. J. Teo, Thermal lattice Boltzmann flux solver and its application for simulation of incompressible thermal flows, *Comput. Fluids* **94**, 98 (2014).
- [31] Y. Wang, C. Shu, C. J. Teo, J. Wu, and L. M. Yang, Three-dimensional lattice Boltzmann flux solver and its applications to incompressible isothermal and thermal flows, *Commun. Comput. Phys.* **18**, 593 (2015).
- [32] A. Jameson, Time dependent calculations using multigrid with applications to unsteady flows past airfoils and wings, in *AIAA, 10th Computer Fluid Dynamics Conference, Honolulu, Hawaii, 1991-1596* (AIAA, Honolulu, USA, 1991).
- [33] Z. Guo, B. Shi, and C. Zheng, A coupled lattice BGK model for the Boussinesq equations, *Int. J. Numer. Meth. Fluids* **39**, 325 (2002).
- [34] X. He, S. Chen, and G. D. Doolen, A novel thermal model for the lattice Boltzmann method in incompressible limit, *J. Comput. Phys.* **146**, 282 (1998).
- [35] L. M. Yang, C. Shu, W. M. Yang, and J. Wu, Development of an efficient gas kinetic scheme for simulation of two-dimensional incompressible thermal flows, *Phys. Rev. E* **97**, 013305 (2018).
- [36] Y. Peng, C. Shu, and Y. T. Chew, Simplified thermal lattice Boltzmann model for incompressible thermal flows, *Phys. Rev. E* **68**, 026701 (2003).
- [37] C. Shu and H. Xue, Comparison of two approaches for implementing stream function boundary condition in DQ simulation of natural in a square cavity, *Int. J. Heat Fluid Flow* **19**, 59 (1998).
- [38] D. Contrino, P. Lallemand, P. Asinari, and L. S. Luo, Lattice Boltzmann simulations of the thermally driven 2D square cavity at high Rayleigh numbers, *J. Comput. Phys.* **275**, 257 (2014).
- [39] P. Le Quéré, Accurate solutions to the square thermally driven cavity at high Rayleigh number, *Comput. Fluids* **20**, 29 (1991).
- [40] D. A. Mayne, A. S. Usmani, and M. Crapper, H-adaptive finite element solution of high Rayleigh number thermally driven cavity problem, *Int. J. Numer. Meth. Heat Fluid Flow* **10**, 598 (2000).
- [41] C. Shu, Application of differential quadrature method to simulate natural convection in a concentric annulus, *Int. J. Numer. Methods Fluids* **30**, 977 (1999).
- [42] T. H. Kuehn and R. J. Goldstein, An experimental and theoretical study of natural convection in the annulus between horizontal concentric cylinders, *J. Fluid Mech.* **74**, 695 (1976).
- [43] H. M. Badr, Laminar combined convection from a horizontal cylinder-parallel and contra flow regimes, *Int. J. Heat Mass Transf.* **27**, 15 (1984).